

Dirt-cheap Gas Scaling Relations: Using Dust Absorption, Metallicity and Galaxy Size to Predict Gas Masses for Large Samples of Galaxies

Hassen M. Yesuf^{1,2} and Luis C. Ho^{1,3}

¹*Kavli Institute for Astronomy and Astrophysics, Peking University, Beijing 100871, China*

²*Kavli Institute for the Physics and Mathematics of the Universe, The University of Tokyo, Kashiwa, Japan 277-8583*

³*Department of Astronomy, School of Physics, Peking University, Beijing 100871, China*

Abstract

We apply novel survival analysis techniques to investigate the relationship between a number of the properties of galaxies and their atomic (M_{HI}) and molecular (M_{H_2}) gas mass, with the aim of devising efficient, effective empirical estimators of the cold gas content in galaxies that can be applied to large optical galaxy surveys. We find that dust attenuation, A_V , of both the continuum and nebular emission, shows significant partial correlations with M_{H_2} , after controlling for the effect of star formation rate (SFR). The partial correlation between A_V and M_{HI} , however, is weak. This is expected because in poorly dust-shielded regions molecular hydrogen is dissociated by far-ultraviolet photons. We also find that the stellar half-light radius, R_{50} , shows significant partial correlations with both M_{H_2} and M_{HI} . This hints at the importance of environment (e.g., galactocentric distance) on the gas content of galaxies and the interplay between gas and SFR. We fit multiple regression to summarize the median, mean, and the 0.15/0.85 quantile multivariate relationships among M_{H_2} , A_V , metallicity, and/or R_{50} . A linear combination of A_V and metallicity (inferred from stellar mass) or A_V and R_{50} , can estimate molecular gas masses within $\sim 2.5 - 3$ times the observed masses. If SFR is used in addition, M_{H_2} can be predicted to within a factor $\lesssim 2$. In this case, A_V and R_{50} are the two best secondary parameters that improve the primary relation between M_{H_2} and SFR. Likewise, M_{HI} can be predicted to within a factor $\lesssim 3$ using R_{50} and SFR.

Key words: galaxies: ISM, galaxies: star formation, galaxies: evolution, ISM: molecules, ISM: dust, extinction

1. INTRODUCTION

The formation of stars from the cold gas in the interstellar medium (ISM) is a fundamental process of galaxy formation and evolution. The observed tight relationship between star formation rate (SFR) and stellar mass (M_*) in galaxies, known as the star-forming main sequence (Noeske et al. 2007), is interpreted as indicating that galaxies exhibit a self-regulated quasi-equilibrium between external gas accretion, star formation, and gas outflow (Bouché et al. 2010; Dekel et al. 2013; Lilly et al. 2013; Forbes et al. 2014; Peng & Maiolino 2014; Rodríguez-Puebla et al. 2016). However, the mechanisms that regulate the availability of gas for star formation and the efficiency with which it is converted to stars on galactic scales are not well understood. Energy and momentum inputs from massive stars, supernovae, and accreting supermassive black holes may regulate global star formation by driving galactic outflows or heating the ISM (e.g., Dekel et al. 2009; Hopkins et al. 2011; Ostriker & Shetty 2011; Faucher-Giguère et al. 2013; Hopkins et al. 2014; Harrison et al. 2018).

Although gas observations have strong constraining power for theoretical models of galaxy formation and evolution, directly measuring gas properties for large representative galaxy samples is a difficult and time-consuming endeavor. Neutral atomic hydrogen (H I) can be directly observed via the 21 cm hyperfine line, but molecular hydrogen (H_2) must be inferred indirectly from other tracers, such as the rotational transitions of CO. However, measuring these lines for galaxy sample sizes comparable to those of ultraviolet-optical surveys will remain unattainable for the foreseeable future. Blind H I surveys such as the Arecibo Legacy Fast ALFA survey do provide global (unresolved) measurements of the H I content for $\sim 31,500$ galaxies (Haynes et al. 2018), but are only sensitive to the most gas-rich galaxies located

at very modest redshifts ($z \lesssim 0.06$). In contrast, the extended GALEX Arecibo SDSS Survey (xGASS; Catinella et al. 2018) provides more sensitive measurements of atomic gas content for 1179 representative galaxies. A follow-up survey, xCOLD GASS (Saintonge et al. 2017), additionally obtained H_2 measurements for 477 galaxies using the CO (1–0) emission line. Although the GASS samples account for only less than 0.2% of local galaxies, they are large enough to statistically characterize gas scaling relations and their scatter. Saintonge et al. (2017) and Catinella et al. (2018) showed that typical state-of-the-art hydrodynamic and semi-analytic simulations, which currently implement sub-grid ISM models, do not succeed in reproducing the gas scaling relations based on the GASS data. But encouraging progress is being made (e.g., Diemer et al. 2019). In a similar spirit, pushing out to much greater distances, the Plateau de Bure High- z Blue Sequence Survey (Freundlich et al. 2019) legacy program collected CO data of ~ 120 galaxies at $z = 0.5 - 3$. Detecting H I beyond the local universe remains challenging. Concerted efforts are being made with current interferometers, but the current samples remain frustratingly small (Verheijen et al. 2007; Hess et al. 2019); the most distant H I detection to date is at $z = 0.316$ (Fernández et al. 2016).

An alternative, albeit indirect, method to probe the gas content of galaxies is to estimate the dust mass from the far-infrared emission and convert it to gas mass using a gas-to-dust ratio. Dust is an important constituent of the ISM, and it has a huge impact on the chemistry and thermodynamics of the gas (Krumholz et al. 2011; Glover & Clark 2012; Gong et al. 2017). Dust shields molecules (e.g., CO) from photodissociation by attenuating the interstellar far-ultraviolet radiation field. The atomic-to-molecular hydrogen transition is governed by the balance between H_2 formation via dust grain catalysis and destruction by ultraviolet photons from the Lyman-Werner band. With the advent of the *Herschel Space Observatory* and the Atacama Large Millimeter Array, dust continuum emission has been utilized in numerous studies as a surrogate tool to estimate gas masses (e.g., Eales et al. 2012; Genzel et al. 2015; Groves et al. 2015; Scoville et al. 2016; Janowiecki et al. 2018; Shanguan et al. 2018, 2019). The far-infrared emission, however, is not a simple tracer; there are major systematic uncertainties or modeling challenges to exploiting it as a probe of gas content of galaxies (e.g., Berta et al. 2016). And rest-frame far-infrared measurements, while more widely available than H I or CO observations, are still non-trivial to amass for large galaxy samples.

This paper introduces new, efficient, and cost-effective methods to predict gas masses within a factor of $\sim 2 - 3$ for large samples of galaxies. To that end, we revisit the relationship between the integrated gas mass, SFR, and galaxy morphology of the well-studied local galaxies in the xGASS and xCOLD GASS surveys (Saintonge et al. 2011, 2017; Catinella et al. 2018). We investigate whether parameters such as dust attenuation, galaxy radius, and galaxy morphology are useful in predicting atomic and molecular gas masses. We conclude that the dust extinction A_V of both the continuum and nebular emission significantly correlates with M_{H_2} , after controlling for the effect of SFR. The same does not hold for M_{HI} . We find that R_{50} also significantly correlates with both M_{H_2} and M_{HI} .

2. DATA AND METHODOLOGY

2.1. Stellar and Dust Properties

We use the publicly available Catalog Archive Server (CAS)¹ to retrieve measurements of median stellar mass, galaxy size, and optical emission-line fluxes based on the Sloan Digital Sky Survey (SDSS) data release 15 (Aguado et al. 2019). We use the median metallicity estimate given in `galSpecExtra` table for non-AGN galaxies whose principal optical diagnostics emission-line ratios are measured at $> 5\sigma$. These data are supplemented with global measurements of V -band dust attenuation (A_V) and SFR from version 2 of the GALEX-SDSS-WISE Legacy Catalog (GSWLC-2; Salim et al. 2016, 2018), along with improved galaxy morphology measurements, derived using machine learning, from Domínguez Sánchez et al. (2018). Salim et al. (2016, 2018) used spectral energy distribution fitting of ultraviolet, optical, and infrared photometry to calculate the global A_V and SFR. To estimate accurate total infrared luminosities (~ 0.1 dex uncertainty), Salim et al. (2018) used luminosity-dependent infrared templates (Chary & Elbaz 2001) and calibrations derived from a subset of galaxies that have far-infrared photometry from the *Herschel* ATLAS survey. They assumed a Chabrier (2003) stellar initial mass function. By combining accurate visual classifications from the Galaxy Zoo 2 project (Willett et al. 2013) and machine-based classifications from Nair & Abraham (2010), Domínguez Sánchez et al. (2018) provided one of the largest and most reliable ($\gtrsim 97\%$ accuracy) morphological catalogs for the SDSS galaxies. Their classifications apply the convolutional neural networks learning algorithm to reanalyze the SDSS three-color galaxy images to learn the mapping between the images and the measurements in the visual classification catalogs, and also to correct misclassifications in the visual catalogs. The measurements from Domínguez Sánchez et al. (2018) that we use are the T-types and a set of probabilities that quantify whether a galaxy has a disk/feature or

¹ <http://skyserver.sdss.org/casjobs/>

a bar, and whether it is an edge-on system or a merger. The T-types range from -3 to 10 , whereby 0 corresponds to S0s, < 0 corresponds to early-type galaxies, > 0 corresponds to spirals (Sa–Sm), and 10 represents irregular galaxies. The disk/feature probability quantifies whether a galaxy is smooth or has a disk or features such as spiral arms.

We calculate the fiber V -band attenuation using the observed $H\alpha/H\beta$ ratio and the dust attenuation curve, as (Charlot & Fall 2000; Wild et al. 2011)

$$Q_\lambda = 0.6 (\lambda/5500)^{-1.3} + 0.4 (\lambda/5500)^{-0.7}. \quad (1)$$

Assuming that the intrinsic, dust-free Balmer decrement is $H\alpha/H\beta = 2.86$ for inactive galaxies and $H\alpha/H\beta = 3.1$ for active galactic nuclei (AGNs; e.g., Ferland & Netzer 1983; Gaskell & Ferland 1984),

$$A_{V,\text{fiber}} = \frac{2.5}{(Q_{4861} - Q_{6563})} \times \log \frac{H\alpha/H\beta}{3.1 \text{ or } 2.86}. \quad (2)$$

where $Q_{4861} - Q_{6563} = 0.31$. If the observed ratio of an object is below the intrinsic ratio, we set $A_{V,\text{fiber}} = 0$.

2.2. Atomic and Molecular Gas Properties

We use the publicly available atomic gas data from xGASS² and molecular gas data from xCOLD GASS³. xGASS observed the H I properties of 1179 representative galaxies from SDSS DR7, selected based only on stellar mass ($M_\star = 10^9 - 10^{11.5} M_\odot$) and redshift ($z = 0.01 - 0.05$). xCOLD GASS is a follow-up survey, which observed the CO (1–0) emission of 532 galaxies using the IRAM 30 m radio telescope. The CO emission is converted to molecular hydrogen mass (given in the catalog) using a conversion factor (X_{CO}) that depends on the gas-phase metallicity and the offset of a galaxy from the star-forming main sequence (Accurso et al. 2017). We note that the uncertainties on M_{H_2} are large because of uncertainties of aperture correction of single-beam CO observations and of the X_{CO} factor. Our main results do not change if we use the constant Galactic X_{CO} . The overlap between the xCOLD GASS and the xGASS samples includes 477 galaxies, among which 368 have reliable $H\alpha$ and $H\beta$ ($> 3\sigma$) measurements and 290 were detected in CO. Whenever A_V is used, we require it to be well-measured ($> 3\sigma$) either from the Balmer decrement or from SED fitting.

2.3. Statistical Methods

We apply survival analysis methods (Feigelson & Nelson 1985; Helsel 2012) to analyze data that include both gas detections and upper limits. Kendall’s τ is a non-parametric (rank-based) correlation coefficient, which can be used to quantify a monotonic association (linear or nonlinear) between two variables for both censored and uncensored data (Helsel 2012). The quantity τ is the probability of concordance minus the probability of discordance for randomly selected pairs of observations. It ranges between -1 and 1 : $\tau = 1$ is a perfect correlation; $\tau = 0$ is no correlation; and $\tau = -1$ is a perfect inverse correlation. Following Yesuf et al. (2017), we compute the Kendall’s τ coefficient using the `cenken` routine in the NADA R package⁴ (Helsel 2012).

If the Kendall’s τ between a galaxy property and the gas mass is significantly different from 0, we use a partial correlation test to investigate possible additional associations with other parameters. The partial correlation test quantifies the degree of association between two variables after controlling for the effect of a third variable (Akritas & Siebert 1996)⁵. After identifying several parameters that strongly correlate with the molecular or atomic gas masses using the partial correlation test, we fit the association between three or more variables using a censored multiple regression. In particular, we use a censored quantile regression (Portnoy 2003) to describe the median and the 0.15 and 0.85 quantile variability of the gas mass trends. In contrast to standard linear regression, quantile regression does not assume that the residuals are normally distributed around the mean, and it provides a richer characterization of the variability in the data by quantifying the effects of covariates on the whole distribution of the dependent variable, not just the mean trend. We use the `cqr` routine in the `quantreg` R package⁶ to fit the censored quantile regression model and estimate the coefficients that describe the quantile relations. The routine also gives the standard errors of the coefficients using bootstrap resampling. For comparison, we also fit for the mean trends using the `cenreg` routine in the NADA R package, which computes the regression coefficients using maximum likelihood estimation and

² <http://xgass.icrar.org/data.html>

³ <http://www.star.ucl.ac.uk/xCOLDGASS/>

⁴ <https://CRAN.R-project.org/package=NADA>

⁵ <http://astrostatistics.psu.edu/statcodes/cens.tau>

⁶ <https://CRAN.R-project.org/package=quantreg>

Table 1. Kendall’s τ correlation and partial correlation coefficients between gas mass and galaxy properties.

Galaxy Property	τ_{H_2}	$\tau_{\text{H}_2} \mid A_V$	$\tau_{\text{H}_2} \mid \text{SFR}$	$\tau_{\text{H}_2} \mid R_{50}$	τ_{HI}	$\tau_{\text{HI}} \mid \text{SFR}$	$\tau_{\text{HI}} \mid R_{50}$	Significance
Fiber (nebular) dust attenuation A_V	0.39	—	0.24	0.38	0.16	0.04	0.14	✓—✓✓✓✓✓
Global (stellar) dust attenuation A_V	0.41	0.25	0.21	0.41	0.23	0.01	0.21	✓✓✓✓✓ X ✓
Global SFR	0.58	0.54	—	0.58	0.46	—	0.41	✓✓—✓✓—✓
Petrosian radius R_{50}	0.32	0.32	0.19	—	0.35	0.24	—	✓✓✓—✓✓—
Petrosian radius R_{90}	0.27	0.29	0.19	0.03	0.29	0.21	0.01	✓✓✓ X ✓✓ X
Stellar mass M_*	0.18	0.24	0.19	0.08	0.09	0.10	−0.08	✓✓✓ X ✓✓✓
Disk/feature probability $P_{\text{d/f}}$	0.30	0.21	0.10	0.19	0.37	0.26	0.28	✓✓✓✓✓✓✓
T-type	0.23	0.11	0.04	0.16	0.30	0.20	0.27	✓✓ X ✓✓✓✓
Bar probability	0.19	0.14	0.03	0.12	0.22	0.12	0.16	✓✓✓ X ✓✓✓
Concentration index R_{90}/R_{50}	−0.20	−0.11	−0.04	−0.17	−0.18	−0.08	−0.18	✓✓ X ✓✓✓✓
Mass density $0.5M_*/(\pi R_{50}^2)$	−0.20	−0.14	−0.17	−0.03	−0.10	0.03	−0.03	✓✓✓ X ✓ X X
Edge-on probability	−0.09	−0.16	~ 0.00	−0.03	−0.07	−0.02	−0.02	✓✓ X X X X X
Merger probability	0.04	0.08	~ 0.01	~ 0.01	0.01	0.01	~ 0.00	X X X X X X

NOTE— τ_{H_2} and τ_{HI} are Kendall’s τ rank-correlation coefficient for the molecular and atomic gas, respectively. $\tau_y \mid x : x \in \{A_V, \text{SFR}, R_{50}\} \& y \in \{\text{H}_2, \text{HI}\}$ are the partial Kendall’s τ coefficients, after removing the effect of dust attenuation (nebular) or SFR or the half-light radius. The significance of each correlation or partial correlation is indicated in the last column, in the order of the preceding columns: ✓ denotes that the probability of the null hypothesis $\tau = 0$ (no correlation or partial correlation) being correct is $p < 0.001$; **X** denotes that this probability is higher and the null hypothesis cannot be rejected at $> 3\sigma$. The T-types range from −3 to 10: ≤ 0 corresponds to early-type and S0 galaxies; > 0 corresponds to spiral galaxies.

tests for their significance. We assume a normal distribution for this calculation but have checked that the results are not sensitive to this assumption using the Buckley-James distribution-free least-squares multiple regression model, as implemented in the `rms` R package⁷.

3. RESULTS

3.1. Predictors of Molecular Gas Mass

Table 1 summarizes the correlation and partial correlation analysis between the molecular or atomic gas and other galaxy properties. The integrated SFR, A_V , galaxy size, and disk/feature probability are among the galaxy properties that exhibit high Kendall’s τ correlation coefficients ($\tau \geq 0.3$) with the gas mass. As expected, SFR shows the strongest correlation with gas content ($\tau = 0.58$ for M_{H_2} ; $\tau = 0.46$ for M_{HI}). We find a moderately strong ($\tau \approx 0.4$) but highly significant ($> 5\sigma$) correlation between global or fiber A_V and M_{H_2} . A_V correlates better with M_{H_2} than with M_{HI} , or the combination of the two. The partial correlation analysis indicates that there is a highly significant correlation between A_V and M_{H_2} ($\tau \approx 0.2$), *after* controlling for the effect of the SFR. In contrast, the partial correlation between A_V and M_{HI} is very weak and hardly statistically significant. The stellar r -band half-light radius of the galaxy, R_{50} , also has a partial $\tau \approx 0.2$ with both M_{H_2} and M_{HI} at fixed SFR. However, the correlation between R_{50} and A_V is weak ($\tau = 0.1$), which implies that controlling for the effect of the other hardly changes the partial correlation with the gas mass. After controlling for A_V , M_* shows significant partial correction ($\tau = 0.24$). This could be anticipated from the mass-metallicity relation (Tremonti et al. 2004) and from the dependence of dust-to-gas ratios on metallicity (e.g., Janowiecki et al. 2018). It is not so obvious why R_{50} is better correlated ($\tau = 0.32$) with M_{H_2} after fixing A_V . This correlation may reflect the association of R_{50} with metallicity and its deviation from the mass-metallicity relation (Tremonti et al. 2004), and the processes that set the molecular-to-atomic gas ratio or gas mass to SFR ratio (i.e., the star formation efficiency). The disk/feature probability ($P_{\text{d/f}}$) shows a partial correlation of $\tau \approx 0.3$ with M_{HI} after controlling for SFR or R_{50} . After controlling for SFR, no significant correlation exists between molecular/atomic gas mass and the stellar concentration index, stellar surface mass density, or merger or edge-on probability. The atomic gas partially correlates with T-type ($\tau = 0.2$), given the SFR.

Next, we fit the relationship between gas mass and galaxy properties that show strong statistical correlation. Tables 2–4 (the latter two are in Appendices A and B) present the result of fitting a censored quantile regression ($q = 0.15$,

⁷ <https://CRAN.R-project.org/package=rms>

0.5, and 0.85) or a normal censored linear regression model to the xCOLD GASS molecular mass data (Saintonge et al. 2017). In Table 2, the coefficients of the equations describing the relationship among molecular gas mass, dust attenuation, gas-phase metallicity (Z) and/or galaxy radius are given. We infer Z from the mass-metallicity relation of Tremonti et al. (2004). We present two sets of fits, using either the global (stellar) attenuation or the fiber (nebular) attenuation. Although the scatter is modeled by the $q = 0.15$ and 0.85 regression fits, we additionally quantify the scatter for each relationship using the root mean square deviation (RMSD) and the median absolute deviation (MAD). For normally distributed residuals, $\text{RMSD} \approx 1.48 \text{ MAD}$. The calculations of MAD and RMSD include the detections but not the upper limits, and these measures should be regarded as approximate indicators of the true scatter. Table 3 repeats the analysis for the constant Galactic X_{CO} . Both cases give consistent fitting formulae.

As shown in Figures 1 and 2, M_{H_2} can be indirectly estimated (within a factor of ~ 2.5) for a large sample of galaxies using A_V and Z , as follows:

$$\log M_{\text{H}_2} = \alpha + \beta_A A_V + \beta_Z \log Z, \quad (3)$$

where $\log Z = 12 + \log [\text{O}/\text{H}] - 8.8$, $(\alpha, \beta_A, \beta_Z) = (8.27 \pm 0.11, 0.38 \pm 0.13, 1.44 \pm 0.34)$ for fiber (nebular) A_V , and $(\alpha, \beta_A, \beta_Z) = (8.23 \pm 0.12, 0.91 \pm 0.36, 1.30 \pm 0.31)$ for global (stellar) A_V . Note that the continuum attenuation is ~ 2 times lower than the nebular attenuation (Calzetti et al. 1994; Wild et al. 2011). This may explain the lower β_A in the case of fiber A_V . M_{H_2} can be similarly related to A_V and R_{50} :

$$\log M_{\text{H}_2} = \alpha + \beta_A A_V + \beta_R \log R_{50}, \quad (4)$$

where $(\alpha, \beta_A, \beta_R) = (7.84 \pm 0.09, 0.42 \pm 0.06, 1.27 \pm 0.09)$ for fiber A_V and $(\alpha, \beta_A, \beta_R) = (7.58 \pm 0.11, 1.41 \pm 0.13, 1.35 \pm 0.19)$ for global A_V .

The linear combination of A_V and M_\star also has comparable predictive power, but it does not constrain well the scatter from its mean relation. For the mean or median gas relations, however, the coefficients corresponding to M_\star , Z , and R_{50} are all significant at $\alpha = 0.05$. The Akaike information criterion (AIC) and the Bayesian information criterion (BIC), which adjust the likelihood/penalize for the extra parameters, indicate that the normal censored regression model that combines A_V with either Z or M_\star or R_{50} is preferred over A_V by itself. Furthermore, using the inferred mean metallicity from the mass-metallicity relation (e.g., equation 3 of Tremonti et al. (2004)), the gas masses predicted by equation 3 above agree within a factor of ~ 2.5 with observed M_{H_2} of all detections in xCOLD GASS ($\text{MAD} = 0.22$ and $\text{RMSD} = 0.36$). Thus, this equation may be applied to large samples of galaxies with indirect metallicity estimates. Because the metallicity is measured only for strong emission-line star-forming galaxies, when applying the relation to weak emission-line galaxies, users should verify whether other scaling relations give similar M_{H_2} estimates. The relation that adds R_{50} to equation 3 (see Table 2) or just combines A_V and R_{50} (equation 4) gives a complementary gas mass estimate in such cases.

It is customary to use SFR as a predictor of gas content, especially for high-redshift studies (e.g., Boselli et al. 2014b; Popping et al. 2015; Saintonge et al. 2017; Catinella et al. 2018). As shown in Table 4 and Figure 3 in Appendix B, adding SFR to equation 4 improves the fit significantly. This table also gives detailed information for various fits when one or more variables are missing or may not be desirable to include. All these combinations can predict gas mass within a factor of ~ 3 . Users should be careful not to use these relations in a circular manner. For example, if SFR is already used by a scaling relation to get M_{H_2} , such a scaling relation should not be employed to study the correlation between M_{H_2} and SFR. Users should also take into account the quartile relations in the gas mass estimation, as there are systematic trends in the scatters of the scaling relations.

In summary, dust attenuation is significantly correlated with the molecular gas mass. A linear combination of A_V and metallicity or A_V and R_{50} can indirectly estimate molecular gas masses within $\sim 2.5 - 3$ times the observed masses. If SFR is further used, M_{H_2} can be predicted to within a factor $\lesssim 2$. In this case, A_V and R_{50} are the two best secondary parameters that improve the primary correlation between M_{H_2} and SFR.

3.2. Predictors of Atomic Gas Mass

For xGASS data (Catinella et al. 2018), the atomic gas mass can be predicted within a factor of ~ 2.5 from the SFR and half-light radius (equation 5). Table 5 in Appendix B presents the result of fitting censored regression models to the xGASS data, describing the relationship among the atomic gas mass, SFR, the half-light radius, T-type, disk/feature probability, and/or dust attenuation. We present two sets of fits, by analyzing the central and satellite

Table 2. Regression model fits for molecular gas, $\log M_{\text{H}_2} = \alpha + \beta_A A_V + \beta_Z \log Z + \beta_R \log R_{50}$.

	Nebular $A_{V,\text{Fiber}}$				Stellar $A_{V,\text{Global}}$			
	15%	Median	85%	Mean	15%	Median	85%	Mean
α	7.70 ± 0.07	8.31 ± 0.04	8.91 ± 0.06	8.34 ± 0.04	7.63 ± 0.22	8.04 ± 0.09	8.71 ± 0.12	8.12 ± 0.05
β_A	0.47 ± 0.05	0.47 ± 0.02	0.38 ± 0.05	0.43 ± 0.03	1.52 ± 0.20	1.58 ± 0.13	1.39 ± 0.27	1.49 ± 0.10
Scatter		0.31		0.50		0.35		0.49
α	8.05 ± 0.08	8.27 ± 0.11	8.56 ± 0.07	8.30 ± 0.05	7.96 ± 0.03	8.23 ± 0.12	8.59 ± 0.11	8.21 ± 0.06
β_A	0.25 ± 0.10	0.38 ± 0.13	0.38 ± 0.04	0.31 ± 0.05	1.10 ± 0.06	0.91 ± 0.36	0.91 ± 0.30	0.90 ± 0.13
β_Z	1.29 ± 0.36	1.44 ± 0.34	1.67 ± 0.19	1.56 ± 0.20	—	1.30 ± 0.31	1.65 ± 0.26	1.46 ± 0.20
Scatter		0.22		0.37		0.24		0.35
α	7.41 ± 0.10	7.84 ± 0.09	8.49 ± 0.10	7.95 ± 0.05	7.48 ± 0.09	7.58 ± 0.11	8.16 ± 0.05	7.70 ± 0.06
β_A	0.35 ± 0.06	0.42 ± 0.06	0.35 ± 0.04	0.37 ± 0.03	1.24 ± 0.29	1.41 ± 0.13	1.34 ± 0.14	1.34 ± 0.08
β_R	1.34 ± 0.28	1.27 ± 0.09	0.89 ± 0.12	1.11 ± 0.09	0.97 ± 0.09	1.35 ± 0.19	1.12 ± 0.10	1.19 ± 0.08
Scatter		0.25		0.41		0.26		0.38
α	7.87 ± 0.07	8.07 ± 0.06	8.56 ± 0.07	8.16 ± 0.06	7.74 ± 0.13	7.98 ± 0.07	8.41 ± 0.18	8.02 ± 0.07
β_A	0.24 ± 0.03	0.35 ± 0.06	0.38 ± 0.04	0.31 ± 0.05	1.09 ± 0.16	0.91 ± 0.11	0.98 ± 0.18	0.96 ± 0.12
β_Z	0.95 ± 0.35	1.40 ± 0.15	1.67 ± 0.19	1.29 ± 0.20	—	0.98 ± 0.23	1.13 ± 0.37	1.02 ± 0.20
β_R	0.63 ± 0.12	0.56 ± 0.15	—	0.48 ± 0.12	0.63 ± 0.18	0.74 ± 0.11	0.50 ± 0.22	0.62 ± 0.12
Scatter		0.21		0.35		0.25		0.33

NOTE—The coefficients of the equations describe the relationship among molecular gas mass (M_{H_2}), dust attenuation (A_V), metallicity ($\log Z = 12 + \log [\text{O}/\text{H}] - 8.8$), and/or galaxy radius (R_{50}). Fits are given for the attenuation in the fiber ($A_{V,\text{fiber}}$) and galaxy-wide attenuation ($A_{V,\text{global}}$). We give two measures of the scatter for the fits: the median absolute deviation (MAD, the left numbers corresponding to the median fits) and the root mean square deviation (RMSD, the right numbers corresponding to the mean fits). $\text{MAD} = \text{median}(|Y_i - \bar{Y}|)$, where $Y_i = \log M_{\text{H}_2}$ is the i th observed molecular gas mass and \bar{Y} is the fitted median relation. Similarly, $\text{RMSD} = \sqrt{\text{mean}((Y_i - \bar{Y})^2)}$, where \bar{Y} is the fitted mean relation. The fits that include $\log Z$ are based solely on strong emission-line starforming galaxies. They give reasonable prediction when the metallicity is estimated from the stellar mass for all galaxies (see Figure 1).

galaxies together, or by restricting the sample to central galaxies only. The classification of satellites and centrals is based on the galaxy group catalog of Yang et al. (2007). The median fit for the whole sample is

$$\log M_{\text{HI}} = \alpha + \beta_S \log \text{SFR} + \beta_R \log R_{50}, \quad (5)$$

where $(\alpha, \beta_S, \beta_R) = (9.07 \pm 0.04, 0.47 \pm 0.02, 1.08 \pm 0.11)$. The regression coefficients for central galaxies alone are consistent with those for the total sample. In comparison, the corresponding median relation for the molecular gas yields $(\alpha, \beta_S, \beta_R) = (8.77 \pm 0.05, 0.81 \pm 0.03, 0.46 \pm 0.11)$. The molecular gas has weaker dependence on radius. Hence, the atomic-to-molecular ratio depends on R_{50} . Table 5 also gives three other scaling relations that can predict gas mass with accuracy of a factor ~ 3 without using SFR but combining R_{50} with either T-type or disk/feature probability or dust attenuation.

For completeness, we give the relations for the total gas mass ($M_{\text{HI}} + M_{\text{H}_2}$), $\log M_{\text{gas}} = \alpha + \beta \log R_{50} + \gamma \log \text{SFR}$, using galaxies contained in both the xGASS and xCOLD GASS surveys. The median relation yields $\alpha = 9.28 \pm 0.04$, $\beta = 0.87 \pm 0.11$, and $\gamma = 0.70 \pm 0.04$; for $q = 0.15$, $\alpha = 8.83 \pm 0.05$, $\beta = 1.05 \pm 0.07$, and $\gamma = 0.88 \pm 0.02$; and for $q = 0.85$, $\alpha = 9.55 \pm 0.05$, $\beta = 0.85 \pm 0.11$, and $\gamma = 0.59 \pm 0.07$.

4. DISCUSSION

Dust is often used to estimate indirectly the gas content in galaxies (e.g., Devereux & Young 1990). We find that dust attenuation, A_V , is significantly correlated with the molecular gas mass, M_{H_2} . A linear combination of A_V and metallicity or A_V and R_{50} can indirectly estimate M_{H_2} within $\sim 2.5 - 3$ times the observed masses. However, the correlation between A_V and M_{HI} is weak. A combination of R_{50} and SFR can give an estimate of M_{HI} accurate to within a factor of ~ 3 . Next, we briefly discuss previous studies that aid the interpretation of our results. We surmise that the correlation of M_{H_2} with metallicity and R_{50} likely comes from physical processes that determine the gas-to-dust ratio and molecular gas fraction.

The ratio of dust mass to total gas mass ($\xi = \mu M_{\text{H}}/M_{\text{dust}}$, where $M_{\text{H}} = M_{\text{HI}} + M_{\text{H}_2}$ and the correction factor for helium $\mu \approx 1.4$) varies approximately linearly with metallicity ($\log \xi \propto \beta \log Z \propto \beta \log [\text{O}/\text{H}]$) such that higher metallicity galaxies have lower ξ (Issa et al. 1990; Lisenfeld & Ferrara 1998; Draine et al. 2007; Galametz et al. 2011; Leroy et al. 2011; Brinchmann et al. 2013; Berta et al. 2016; De Vis et al. 2019). The amount of dust along a line of sight can be estimated using dust attenuation A_V , while the amount of gas is probed by the total hydrogen column density N_{H} . A_V/N_{H} can then be used to infer the dust-to-gas ratio. It is known that A_V/N_{H} positively correlates with metallicity in nearby galaxies (e.g., Kahre et al. 2018). Therefore, it is natural to anticipate that the molecular gas mass depends on both A_V and metallicity. If $f_{\text{H}_2} \equiv M_{\text{H}_2}/M_{\text{H}}$ and $R_{\text{H}_2} \equiv M_{\text{H}_2}/M_{\text{HI}}$, then the molecular mass can be expressed as:

$$M_{\text{H}_2} = M_{\text{H}} \times M_{\text{H}_2}/M_{\text{H}} = \xi \mu^{-1} M_{\text{dust}} f_{\text{H}_2} = \xi \mu^{-1} M_{\text{dust}} (1 + R_{\text{H}_2}^{-1})^{-1} \quad (6)$$

Because previous observations indicate $\xi \propto Z^{\beta_\xi}$ and $R_{\text{H}_2} \propto Z^{\beta_{R_{\text{H}_2}}}$, M_{H_2} depends on both dust mass and metallicity. Depending on the metallicity calibration, X_{CO} , and sample selection, $\beta_\xi \approx -0.7$ to -2.5 (Issa et al. 1990; Muñoz-Mateos et al. 2009; Leroy et al. 2011; Rémy-Ruyer et al. 2014; Janowiecki et al. 2018; De Vis et al. 2019) and $\beta_{R_{\text{H}_2}} \approx 2.7 - 3.4$ (Boselli et al. 2014b). Furthermore, we expect that f_{H_2} and R_{H_2} also depend on R_{50} . We showed in Section 3.2 that M_{H_2} and M_{HI} scale differently with R_{50} . Based on the empirical correlation between mid-plane gas pressure of galactic disks and R_{H_2} (e.g., Blitz & Rosolowsky 2006), Obreschkow & Rawlings (2009) presented a phenomenological model that predicts that $R_{\text{H}_2} \propto M_{\text{H}}^{-0.24} \propto R_{50}^{-0.39}$. If $f_{\text{H}_2} \propto R_{50}^{\beta'_R} Z^{\beta'_Z}$, then equation 6 implies that $\log M_{\text{H}_2} \propto \log M_{\text{dust}} + \beta'_R \log R_{50} + \beta'_Z \log Z$, where $\beta_Z = \beta_\xi + \beta'_Z$. For galaxies in the Herschel Reference Survey (HRS), Janowiecki et al. (2018) found $\beta_\xi = -0.72 \pm 0.19$ and $\beta_Z = 0.67 \pm 0.26$ (without including the R_{50} term; see equations in their Section 2.2). In other words, they found a negative correlation between metallicity and gas-to-dust ratio defined using the total gas phase (ξ) or H I ($\xi^{\text{HI}} = M_{\text{HI}}/M_{\text{dust}}$), but a positive correlation using H_2 ($\xi^{\text{H}_2} = M_{\text{H}_2}/M_{\text{dust}}$). Their $\xi^{\text{HI}} - Z$ relationship has the highest correlation coefficient ($|r| = 0.50 \pm 0.08$) while their relationship with ξ has the smallest scatter ($\sigma = 0.23$). The correlation of metallicity with ξ^{H_2} is weak ($r = 0.29 \pm 0.09$; see their Figure 1 for all three correlations). Likewise, Bertemes et al. (2018) found $\beta_Z = 0.12$ using $\beta_\xi = -0.85$ (Leroy et al. 2011). Our molecular gas scaling relations (e.g., equation 3) also imply a positive $\xi^{\text{H}_2} - Z$ correlation. When A_V is estimated from $\text{H}\alpha/\text{H}\beta$ in the fiber and $A_V \neq 0$, we find a median relation $\log M_{\text{H}_2} \propto \log A_V + \beta_Z \log Z$ with $\beta_Z = 1.11 \pm 0.26$. In equation 3, we used the term $\beta_A A_V$ in lieu of $\log A_V$ and found $\beta_Z = 1.44 \pm 0.34$. But M_{dust} likely depends not only on A_V (dust column or surface density) but also on galaxy radius.

The radial profile of dust attenuation or dust surface mass density and the dependence of gas-to-dust ratio on galactocentric distance have been well-studied for local galaxies (e.g., Issa et al. 1990; Boissier et al. 2004, 2007; Muñoz-Mateos et al. 2009; Pappalardo et al. 2012; Sandstrom et al. 2013; Smith et al. 2016; Giannetti et al. 2017; Casasola et al. 2017; Chiang et al. 2018; Vilchez et al. 2019). Accordingly, in most galaxies the attenuation decreases with the galactocentric distance. The quantity A_V/N_{H} (or ξ^{-1}) also decreases with radius: it is higher in the central, metal-rich regions than in the outer parts of galaxies (Issa et al. 1990; Kahre et al. 2018). By combining the signal of 110 spiral galaxies in HRS, Smith et al. (2016) detected dust emission out to about twice the optical radius. They found that the radial distribution of dust is consistent with an exponential, $\Sigma_d(r) = \Sigma_0 10^{\alpha_r r}$, with a gradient of $\alpha_r = 1.7 \text{ dex}/r_{25}$. Here r is the galactocentric radius and r_{25} is the optical radius at the 25 mag arcsec $^{-2}$ isophote. Moreover, Σ_d declines with radius at a similar rate to the stellar mass surface density but more slowly than the surface density of molecular gas or star formation rate (Schruba et al. 2011; Bigiel & Blitz 2012; Smith et al. 2016, see Table 1 of the latter work). Schruba et al. (2011) showed that the CO radial profiles have exponential distributions with a gradient of $\alpha_r = -2.2 \text{ dex}/r_{25}$. Similarly, using galaxies in the H I Nearby Galaxy Survey, Bigiel & Blitz (2012) showed that the total H I and H_2 gas profiles of these galaxies follow exponential distributions beyond the inner 20% of the optical radius with a gradient of $\alpha_r = -0.7 \text{ dex}/r_{25}$. Because mass is the integral of the surface density profile, if the shape of the profile is “universal,” the gas and dust masses of (unresolved) galaxies should vary in a predictable way with the optical radius, consistent with what we found. The origin of the universal gas profile may be related to the halo angular momentum or the radial distribution of the accretion rate (e.g., Mo et al. 1998; Kravtsov 2013; Wang et al. 2014).

For the profile of Smith et al. (2016), $M_{\text{dust}} = 2\pi \int_0^{r_{25}} \Sigma_d(r) r dr \approx 0.4 \Sigma_d(0) r_{25}^2$. Then, for $f_{\text{H}_2} \propto R_{50}^{\beta'_R} Z^{\beta'_Z}$ and $\xi \propto Z^{\beta_\xi}$, equation 6 leads to $M_{\text{H}_2} \propto \beta_A A_V + \beta_R \log R_{50} + \beta_Z \log Z$. Now, β_R is at least $\beta'_R + 2$ and $\beta_Z = \beta_\xi + \beta'_Z$. The conversion of Σ_d to A_V is not straightforward. It depends on radiative transfer effects of the relative geometric

configuration of dust and ionized gas (Calzetti et al. 1994). Kreckel et al. (2013), however, showed that empirical fits to A_V and Σ_d data of local galaxies, with Σ_d expressed in both linear and logarithmic form, can predict Σ_d given A_V to within a factor of ~ 3 . Because in our analysis (Table 2) $\beta_R = 0.56 \pm 0.15$ and $\beta_Z = 1.40 \pm 0.15$, equation 6 implies $f_{\text{H}_2} \propto R_{50}^{\beta'_R} Z^{\beta'_Z}$ if the dust profile of our sample is an exponential, whose scale length is a fixed fraction of R_{50} . Note that combining equations in Janowiecki et al. (2018) for the $\xi^{\text{H}_2} - Z$ and $\xi - Z$ relations gives $\xi^{\text{H}_2}/\xi = f_{\text{H}_2} \propto Z^{1.39 \pm 0.45}$.

Our molecular gas scaling relation likely reflects physics that governs the amount and spatial distribution of dust ($\xi \propto Z^{\beta_\xi}$, $\beta_\xi < 0$) and molecular hydrogen ($f_{\text{H}_2} \propto R_{50}^{\beta'_R} Z^{\beta'_Z}$, $\beta'_Z > 0$ and $\beta'_R < 0$) in the ISM. We believe that it can usefully constrain theoretical models of galaxy formation and evolution. The observed $\xi - Z$ relation has been useful to constrain dust evolution models (e.g., Lisenfeld & Ferrara 1998; Draine et al. 2007; Mattsson & Andersen 2012; Bekki 2013; Rémy-Ruyer et al. 2014; Zhukovska 2014; Aoyama et al. 2017; Galliano et al. 2018; De Vis et al. 2019; Li et al. 2019; Hou et al. 2019). The models range from analytical models to cosmological hydrodynamic galaxy simulations. They attempt to characterize the complex dust physics by including its production by stellar evolution, growth by accretion of metal in the ISM, destruction by supernova shocks and by thermal sputtering in hot gas, and its dependence on star formation history and gas inflows and outflows. The models are able to reproduce reasonably well the observed $\xi - Z$ relation. They indicate that dust growth in the ISM is crucial, and dust destruction by supernova may greatly influence the chemical evolution of galaxies. Dust-related physical processes, however, have only been self-consistently included in a few simulations. Studying the time evolution of dust and f_{H_2} in galaxies using simulations with a self-consistent model for the formation and evolution of dust and H_2 , Bekki (2013) found that f_{H_2} rapidly increases in the first several Gyr of a star-forming galaxy because of more efficient dust production; it is higher in the inner regions of galaxies than in their outer parts. Regions with low ξ (high dust-to-gas ratio) likely have higher f_{H_2} . The author also broadly reproduced (with a systematic offset) the observed $M_{\text{H}_2} \propto M_{\text{dust}}^{0.77}$ relation, which is based on dust emission of only 35 galaxies in the Virgo cluster (Corbelli et al. 2012). Bekki (2015) suggested that the evolution of dust distributions driven by stellar radiation pressure is important for the evolution of SFR, f_{H_2} , and Z in galaxies.

5. SUMMARY AND CONCLUSIONS

We analyze the atomic and molecular gas masses of local representative galaxies ($M_\star = 10^9 - 10^{11.5} M_\odot$ and $z = 0.01 - 0.05$) from the xGASS and xCOLD GASS surveys (Saintonge et al. 2017; Catinella et al. 2018) in conjunction with a number of galaxy properties derived from SDSS. The central result of this work is that we have discovered remarkable new empirical relations that allow us to predict gas masses easily from galaxy survey data. Using different statistical approaches (partial correlation and censored quantile regression analyses), we provide useful and convenient formulae in Tables 2, 4, and 5 that summarize the median, mean, and 0.15/0.85 quantile multivariate relationships between gas mass and other galaxy properties that correlate best with it.

Our main conclusions are as follows:

- The dust attenuation A_V , of both the stellar continuum and gas emission, is significantly correlated with the molecular gas mass (Kendall's rank coefficient $\tau = 0.4$). After controlling for the effect of the SFR, the dust attenuation is still correlated with the molecular gas. Without using SFR, M_{H_2} can be indirectly estimated (within a factor of ~ 2.5) using A_V and gas-phase metallicity (Z) or A_V and R_{50} (Figures 1 and 2 and Tables 1 and 2). In contrast, the correlation between dust attenuation and the atomic gas mass is weak and may be explained by other covariates such as SFR. This result is theoretically expected since in poorly dust-shielded regions molecular hydrogen is dissociated by the far-ultraviolet photons and the atomic gas dominates.
- The galaxy half-light radius R_{50} is significantly correlated with both molecular and atomic gas (Kendall's $\tau = 0.3$). The correlation is still significant after controlling for the effect of SFR or A_V . In practice, R_{50} can be used with A_V or SFR to predict the atomic and molecular gas mass within a factor of $\sim 2 - 3$ for large samples of galaxies and AGNs (detailed equations are given in Tables 2, 4, and 5).
- Depending on how it is quantified, galaxy morphology may be correlated with the atomic gas. In particular, the disk/feature probability and the T-type show significant correlation with the atomic gas after accounting for the effect of SFR or R_{50} . Combining these morphology indicators with R_{50} (and/or A_V) may be useful in predicting atomic gas masses (Table 5), especially for future AGN studies, as they are easier to measure than the SFR. On the other hand, the merger probability and the edge-on probability have little or no significance in

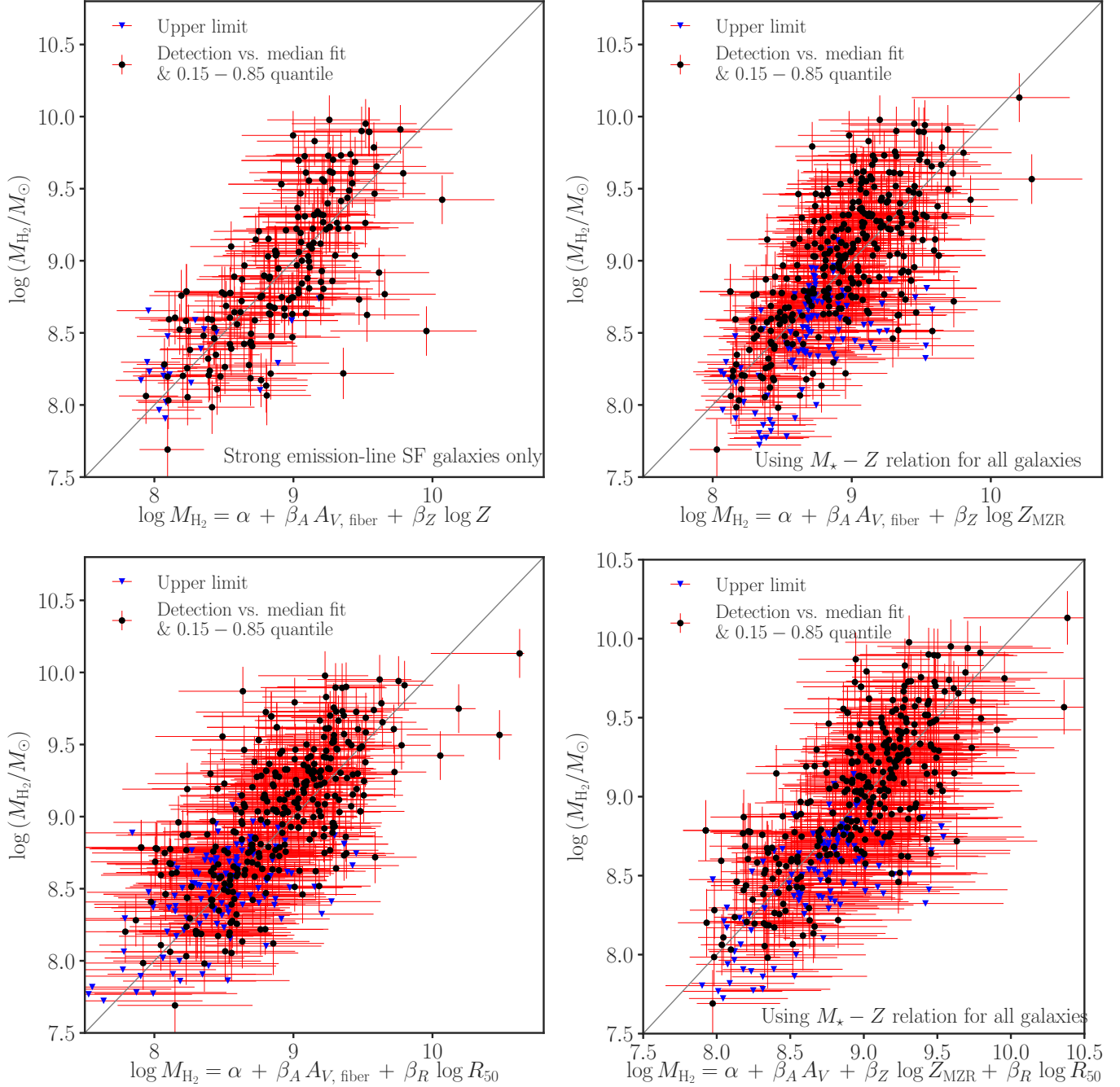


Figure 1. Scaling relations among molecular gas mass (M_{H_2}), fiber A_V , gas-phase metallicity (Z), and half-light radius (R_{50}). The top left panel compares the fitted (predicted) trivariate relation among M_{H_2} , A_V , and Z for star-forming galaxies with strong emission lines (see Table 2). The top right panel shows the same fit applied to the whole sample using metallicity estimates from the mass-metallicity relation (Tremonti et al. 2004). The (black) points denote galaxies with detections, and the (blue) triangles indicate gas mass upper limits, which are included in our analysis. The x-axis positions of the detections and upper limits correspond to the median predictions; the (red) error bars show the predicted 0.15 – 0.85 quantile ranges in the x-axis and the measurement errors of the gas mass in the y-axis. The diagonal (gray) lines are the 1:1 relation. The bottom left panel shows the fitted trivariate relation of M_{H_2} , A_V , and R_{50} for the whole sample. The bottom right panel shows how the prediction from fitting data of the star-forming galaxies generalizes to the whole sample, using metallicity estimates from the mass-metallicity relation. In summary, the figure shows that M_{H_2} can be estimated with accuracy of a factor of ~ 2.5 by combining A_V (Balmer decrement) with Z or R_{50} or both.

explaining the variability in the gas masses of the xGASS sample. The correlations between the molecular gas and all morphology indicators are insignificant, or weak after accounting for the effects of SFR or R_{50} .

As this work was nearing completion, we became aware of a similar effort by [Concas & Popesso \(2019\)](#), who proposed an empirical scaling relation between Balmer decrement and molecular gas mass. They reported a significant correlation between the Balmer decrement and M_{H_2} in a subsample of 222 star-forming galaxies, also from the xCOLD GASS survey. Similar to what we found in Table 1 using the edge-on probability, they showed that star-forming galaxies with high disk inclination angles tend to exhibit high $\text{H}\alpha/\text{H}\beta$ ratios, for the same M_{H_2} , compared to their less inclined counterparts. After correcting for the inclination effect, they did not find residual dependence on galaxy size or star formation rate. This is contrary to what we present in Table 1 for the total xCOLD GASS sample. We show that M_{H_2} is primarily correlated with SFR and secondarily with A_V . Our analysis presented in Appendix C shows that the partial correlation of the inclination angle, i , with M_{H_2} at fixed $\text{H}\alpha/\text{H}\beta$ is much weaker than the corresponding partial correlation of SFR. Likewise, fitting together M_{H_2} , SFR, i , and $\log \text{H}\alpha/\text{H}\beta$ indicates that the inclination angle does not bring additional information, once SFR and $\log \text{H}\alpha/\text{H}\beta$ are used. Using information criteria AIC/BIC and the RMS of the residuals, we conclude that the combination of A_V and Z or A_V and R_{50} is a better predictor of molecular gas than the combination of A_V and i . Unlike the combination of $\text{H}\alpha/\text{H}\beta$ and i proposed by [Concas & Popesso \(2019\)](#), our gas scaling relations work well for all galaxies, star-forming or not, regardless of whether A_V is measured from $\text{H}\alpha/\text{H}\beta$ or stellar continuum absorption.

We note that our atomic and molecular gas scaling relations predict gas masses consistent with independent gas data of galaxies in the Herschel Reference Survey compiled by [Boselli et al. \(2014a\)](#), see Appendix D).

We thank the anonymous referee for helpful comments and suggestions. This work was supported by the National Science Foundation of China (11721303) and the National Key R&D Program of China (2016YFA0400702).

Appendix

A. Checking the Effect of the α_{CO} Assumption

Table 3 repeats Table 2 for the constant Galactic CO conversion factor $\alpha_{\text{CO}} = 4.35 \text{ M}_{\odot} \text{ pc}^{-2} (\text{K km s}^{-1})^{-1}$ (e.g., [Bolatto et al. 2013](#)). The results in the two tables are not significantly different. In other words, there is a significant relationship among molecular gas, metallicity, radius, and dust absorption, $\log M_{\text{H}_2} \propto \beta_A A_V + \beta_R \log R_{50} + \beta_Z \log Z$, whether the metallicity-dependent or the constant α_{CO} is used. Although the difference is not statistically significant, β_Z tend to be higher in the latter case. By definition, the absolute amount of molecular gas depends on α_{CO} . Thus, the intercepts of the scaling relations change with the definition. They are lower for the constant α_{CO} , as expected.

B. Adding SFR, Stellar Mass, and Galaxy Morphology as Gas Mass Predictors

Figure 2 repeats Figure 1 using galaxy-wide stellar A_V instead of nebular A_V . Table 4 extends the analysis in the main section by including SFR and stellar mass as predictors of molecular gas mass, in addition to A_V or/and R_{50} . Figures 3–5 show how the fits change when R_{50} and/or A_V are added to the primary correlation between M_{H_2} and SFR. Figures 6 additionally visualizes the dependence of M_{H_2} on A_V , R_{50} , or metallicity. Figure 7 demonstrates that combining M_{\star} with SFR fails to predict median gas mass for gas-poor galaxies (for xCOLD GASS). When galaxies are on the star formation main sequence, high SFR and high M_{\star} give high gas mass, but when they are off the sequence the relation predicts higher gas mass for high-mass galaxies and overpredicts the gas upper limits. As Table 4 shows, the mass dependence for gas-poor galaxies is weaker (the coefficients change by a factor of 2 and give large changes when multiplied by M_{\star}). The true scatter from the median gas relation predicted by the combination of SFR and M_{\star} is much higher if the upper limits are observed. A priori it is hard to tell which galaxies will be off the median relation. So using this median relation in practice will give less accurate estimates for gas-poor massive galaxies. If SFR is not used, the 0.15 quartile relations (for gas-poor galaxies) seem not to depend on M_{\star} . Table 5 presents details of the atomic gas scaling relations, including ones that combine galaxy size with T-type morphology or disk/feature probability.

C. Galaxy Disk Inclination Angle as a Predictor of Molecular Gas Mass

The aim here is to assess the effects of galaxy inclination on molecular gas mass as proposed by [Concas & Popesso \(2019\)](#). To that end, we take inclination angle (i) measurements from the bulge-disk decomposition catalog of [Simard](#)

Table 3. Regression model fits for molecular gas using constant X_{CO} , $\log M_{\text{H}_2} = \alpha + \beta_A A_V + \beta_Z \log Z + \beta_R \log R_{50}$.

	Nebular $A_{V,\text{Fiber}}$				Stellar $A_{V,\text{Global}}$			
	15%	Median	85%	Mean	15%	Median	85%	Mean
α	7.62 ± 0.06	8.16 ± 0.03	8.99 ± 0.08	8.26 ± 0.05	7.45 ± 0.04	7.92 ± 0.10	8.84 ± 0.08	8.05 ± 0.06
β_A	0.54 ± 0.06	0.63 ± 0.08	0.44 ± 0.06	0.53 ± 0.04	1.85 ± 0.10	1.91 ± 0.16	1.33 ± 0.13	1.74 ± 0.12
Scatter		0.38		0.58		0.45		0.56
α	7.89 ± 0.14	8.01 ± 0.11	8.41 ± 0.02	8.11 ± 0.05	7.73 ± 0.25	7.98 ± 0.05	8.32 ± 0.08	7.98 ± 0.06
β_A	0.20 ± 0.16	0.45 ± 0.10	0.35 ± 0.05	0.32 ± 0.05	1.05 ± 0.63	1.01 ± 0.08	0.99 ± 0.18	1.00 ± 0.13
β_Z	2.46 ± 0.76	2.43 ± 0.42	2.74 ± 0.14	2.61 ± 0.20	1.87 ± 0.47	2.48 ± 0.16	2.74 ± 0.14	2.52 ± 0.20
Scatter		0.23		0.37		0.24		0.34
α	7.15 ± 0.22	7.70 ± 0.07	8.30 ± 0.05	7.76 ± 0.06	7.07 ± 0.16	7.51 ± 0.06	8.01 ± 0.14	7.52 ± 0.06
β_A	0.44 ± 0.10	0.50 ± 0.05	0.42 ± 0.07	0.45 ± 0.03	1.80 ± 0.17	1.48 ± 0.12	1.48 ± 0.27	1.52 ± 0.09
β_R	1.70 ± 0.55	1.51 ± 0.13	1.27 ± 0.08	1.43 ± 0.10	1.29 ± 0.23	1.57 ± 0.09	1.46 ± 0.18	1.52 ± 0.09
Scatter		0.27		0.45		0.24		0.41
α	7.65 ± 0.16	7.90 ± 0.09	8.25 ± 0.07	7.93 ± 0.06	7.55 ± 0.07	7.80 ± 0.03	8.07 ± 0.13	7.74 ± 0.07
β_A	0.26 ± 0.10	0.36 ± 0.10	0.34 ± 0.07	0.32 ± 0.05	1.06 ± 0.10	0.92 ± 0.06	0.93 ± 0.37	1.07 ± 0.11
β_Z	2.02 ± 0.19	2.01 ± 0.48	2.23 ± 0.36	2.23 ± 0.20	1.45 ± 0.29	2.14 ± 0.11	2.44 ± 0.40	1.94 ± 0.19
β_R	0.73 ± 0.44	0.69 ± 0.19	0.56 ± 0.12	0.63 ± 0.12	0.74 ± 0.29	0.72 ± 0.08	0.73 ± 0.18	0.77 ± 0.11
Scatter		0.21		0.34		0.21		0.30

NOTE—Similar to Table 2 except here we adopt the constant Galactic CO-to-H₂ conversion factor $\alpha_{\text{CO}} = 4.35 \text{ M}_\odot \text{ pc}^{-2} (\text{K km s}^{-1})^{-1}$

et al. (2011), in which the bulge Sérsic index was assumed to be $n_b = 4$. For fair comparison, we also use the best SFR estimates from the xCOLD GASS catalog in this section. Here, we focus on star-forming galaxies, since inclination is proposed to be a useful predictor only for these galaxies. Similar to what we showed in Table 1 using the edge-on probability, the partial Kendall τ_{H_2} for the correlation of i with M_{H_2} at fixed $\log \text{H}\alpha/\text{H}\beta$ is -0.15 in star-forming galaxies, while the corresponding partial τ_{H_2} of SFR is 0.64 . Although the partial correlation of i after taking into account the effect of the Balmer decrement is significant (at $\alpha = 0.001$), the strength of its correlation is much smaller than that of SFR. Likewise, given the effect of SFR, the partial τ_{H_2} of i is -0.1 (p value 0.005). In contrast, given i , the partial τ_{H_2} is 0.7 for SFR. Furthermore, fitting together M_{H_2} , SFR, i , and $\log \text{H}\alpha/\text{H}\beta$ with the multiple regression models used in the main text indicates that the coefficient for i is not significant (we fail to reject the null hypothesis that its coefficient is zero at $\alpha = 0.05$). In other words, once SFR and $\log \text{H}\alpha/\text{H}\beta$ are used, i does not carry additional information. Using AIC and BIC also indicates that the normal censored regression model in which M_{H_2} is fitted with SFR and $\log \text{H}\alpha/\text{H}\beta$ describes the data better than the one in which $\log M_{\text{H}_2}$ is fitted with i and $\log \text{H}\alpha/\text{H}\beta$.

Because it has weak but significant partial correlation, it may be useful to include i when SFR measurements are not available. Following Concas & Popesso (2019), fitting the relation $\log M_{\text{H}_2} = a + b(\log \text{H}\alpha/\text{H}\beta - 0.62) + c(i - 56^\circ)$ for star-forming galaxies gives $a = 8.88 \pm 0.03$, $b = 5.70 \pm 0.16$ and $c = -0.007 \pm 0.003$ and $\text{MAD} = 0.22$ dex for the median relation. The mean relation, estimated using the normal censored regression model, has coefficients consistent with those of the median relation and $\text{RMSD} = 0.4$ dex. Our median relation is not inconsistent with the relation of Concas & Popesso (2019). They found $a = 8.93 \pm 0.03$, $b = 5.86 \pm 0.35$ and $c = -0.010 \pm 0.002$. Their fitting does not include star-forming galaxies with M_{H_2} upper limits. Similarly, fitting only the detections with a simulation-extrapolation (SIMEX) weighted least-square model (which includes measurement errors), we get $a = 8.93 \pm 0.03$, $b = 5.09 \pm 0.48$ and $c = -0.008 \pm 0.002$ with RMSD of 0.39 . In contrast, the same statistical model gives RMSD of 0.18 when fitting SFR instead of i . Namely, $\log M_{\text{H}_2} = d + e(\log \text{H}\alpha/\text{H}\beta - 0.62) + f \log \text{SFR}$, where $d = 8.95 \pm 0.14$, $e = 1.92 \pm 0.30$ and $f = 0.80 \pm 0.05$. This gas scaling of star-forming galaxies with SFR and $\text{H}\alpha/\text{H}\beta$ is similar to what we found for the total sample in Section 3. To convert e to the coefficient of $A_{V,\text{fiber}}$, we divide it by 8.06 (from equation 2).

Having established that we get a consistent result to that of Concas & Popesso (2019) for star-forming galaxies, we fit the relation among $\log M_{\text{H}_2}$, i and A_V estimated from the Balmer decrement or stellar continuum. In other words, we add i to the analysis presented in Table 4 and present them in Table 6. After A_V is combined with R_{50} and M_\star , the

Table 4. Regression model fits for molecular gas, $\log M_{\text{H}_2} = \alpha + \beta_A A_V + \beta_R \log R_{50} + \beta_M \log M_\star + \beta_S \log \text{SFR}$.

	Without SFR				With SFR			
	15%	Median	85%	Mean	15%	Median	85%	Mean
α	9.30 ± 0.91	6.62 ± 0.38	6.46 ± 0.36	6.91 ± 0.43	8.44 ± 0.08	6.67 ± 0.21	5.92 ± 0.37	6.34 ± 0.28
$\beta_{A,\text{fiber}}$	0.44 ± 0.07	0.39 ± 0.03	0.29 ± 0.03	0.35 ± 0.03	0.13 ± 0.07	0.16 ± 0.02	0.15 ± 0.02	0.15 ± 0.02
β_R	1.61 ± 0.25	1.13 ± 0.13	0.62 ± 0.06	0.96 ± 0.11	0.34 ± 0.11	0.30 ± 0.05	0.22 ± 0.09	0.29 ± 0.07
β_M	-0.22 ± 0.10	0.13 ± 0.04	0.22 ± 0.04	0.11 ± 0.05	—	0.20 ± 0.02	0.29 ± 0.04	0.23 ± 0.03
β_S	—	—	—	—	0.70 ± 0.09	0.59 ± 0.03	0.53 ± 0.05	0.52 ± 0.02
Scatter		0.23		0.40		0.12		0.24
α	7.41 ± 0.10	7.84 ± 0.09	8.49 ± 0.10	7.95 ± 0.05	8.44 ± 0.08	8.53 ± 0.22	8.69 ± 0.03	8.49 ± 0.04
$\beta_{A,\text{fiber}}$	0.35 ± 0.06	0.42 ± 0.06	0.35 ± 0.04	0.37 ± 0.03	0.13 ± 0.07	0.22 ± 0.02	0.20 ± 0.04	0.20 ± 0.02
β_R	1.34 ± 0.28	1.27 ± 0.09	0.89 ± 0.12	1.11 ± 0.09	0.34 ± 0.11	0.49 ± 0.09	0.73 ± 0.06	0.59 ± 0.07
β_S	—	—	—	—	0.70 ± 0.09	0.61 ± 0.06	0.56 ± 0.05	0.54 ± 0.03
Scatter		0.25		0.41		0.14		0.27
α	7.70 ± 0.07	5.21 ± 0.38	4.44 ± 0.45	5.10 ± 0.41	8.57 ± 0.05	6.05 ± 0.41	5.58 ± 0.33	5.84 ± 0.25
$\beta_{A,\text{fiber}}$	0.47 ± 0.05	0.38 ± 0.05	0.27 ± 0.05	0.35 ± 0.03	0.14 ± 0.06	0.14 ± 0.03	0.14 ± 0.03	0.14 ± 0.02
β_M	—	0.32 ± 0.04	0.44 ± 0.04	0.33 ± 0.04	—	0.27 ± 0.04	0.34 ± 0.03	0.29 ± 0.02
β_S	—	—	—	—	0.75 ± 0.06	0.64 ± 0.05	0.55 ± 0.04	0.55 ± 0.02
Scatter		0.25		0.44		0.12		0.25
α	7.70 ± 0.07	8.31 ± 0.04	8.91 ± 0.06	8.34 ± 0.04	8.57 ± 0.05	8.72 ± 0.06	9.04 ± 0.06	8.76 ± 0.03
$\beta_{A,\text{fiber}}$	0.47 ± 0.05	0.47 ± 0.02	0.38 ± 0.05	0.43 ± 0.03	0.14 ± 0.06	0.23 ± 0.05	0.19 ± 0.03	0.20 ± 0.02
β_S	—	—	—	—	0.75 ± 0.06	0.73 ± 0.03	0.69 ± 0.08	0.63 ± 0.03
Scatter		0.31		0.50		0.16		0.30
α	—	5.20 ± 0.85	3.16 ± 0.53	4.67 ± 0.50	7.47 ± 0.19	6.14 ± 0.16	5.74 ± 0.22	5.83 ± 0.26
β_M	—	0.34 ± 0.09	0.60 ± 0.05	0.39 ± 0.05	0.12 ± 0.02	0.28 ± 0.02	0.34 ± 0.02	0.31 ± 0.02
β_S	—	—	—	—	0.83 ± 0.01	0.78 ± 0.04	0.66 ± 0.04	0.66 ± 0.02
Scatter		0.34		0.61		0.14		0.30
α	—	7.83 ± 0.15	8.70 ± 0.05	8.02 ± 0.05	8.54 ± 0.04	8.77 ± 0.05	8.91 ± 0.08	8.70 ± 0.04
β_R	—	1.84 ± 0.31	1.25 ± 0.07	1.48 ± 0.11	0.35 ± 0.08	0.46 ± 0.10	0.70 ± 0.14	0.59 ± 0.07
β_S	—	—	—	—	0.79 ± 0.06	0.81 ± 0.03	0.69 ± 0.07	0.68 ± 0.03
Scatter		0.36		0.55		0.17		0.31
α	7.48 ± 0.09	7.58 ± 0.11	6.76 ± 0.65	7.04 ± 0.40	8.33 ± 0.15	6.56 ± 0.37	6.16 ± 0.47	6.32 ± 0.27
$\beta_{A,\text{global}}$	1.24 ± 0.29	1.41 ± 0.13	1.28 ± 0.16	1.32 ± 0.08	0.39 ± 0.12	0.41 ± 0.09	0.53 ± 0.09	0.50 ± 0.06
β_R	0.97 ± 0.09	1.35 ± 0.19	0.84 ± 0.16	1.08 ± 0.10	0.49 ± 0.26	0.30 ± 0.10	0.31 ± 0.10	0.37 ± 0.07
β_M	—	—	0.15 ± 0.07	0.07 ± 0.04	—	0.21 ± 0.04	0.26 ± 0.05	0.22 ± 0.03
β_S	—	—	—	—	0.59 ± 0.16	0.61 ± 0.03	0.47 ± 0.05	0.48 ± 0.03
Scatter		0.26		0.38		0.13		0.24
α	7.48 ± 0.09	7.58 ± 0.11	8.16 ± 0.05	7.70 ± 0.06	8.33 ± 0.15	8.51 ± 0.06	8.60 ± 0.13	8.40 ± 0.05
$\beta_{A,\text{global}}$	1.24 ± 0.29	1.41 ± 0.13	1.34 ± 0.14	1.34 ± 0.08	0.39 ± 0.12	0.44 ± 0.08	0.58 ± 0.20	0.57 ± 0.07
β_R	0.97 ± 0.09	1.35 ± 0.19	1.12 ± 0.10	1.19 ± 0.08	0.49 ± 0.26	0.60 ± 0.06	0.83 ± 0.13	0.69 ± 0.07
β_S	—	—	—	—	0.59 ± 0.16	0.61 ± 0.06	0.47 ± 0.06	0.49 ± 0.03
Scatter		0.26		0.38		0.15		0.27
α	7.70 ± 0.07	5.37 ± 0.32	4.30 ± 0.20	4.96 ± 0.38	8.57 ± 0.08	6.40 ± 0.19	5.27 ± 0.15	5.72 ± 0.25
$\beta_{A,\text{global}}$	0.47 ± 0.05	1.49 ± 0.14	1.17 ± 0.15	1.38 ± 0.09	0.31 ± 0.15	0.39 ± 0.05	0.50 ± 0.09	0.43 ± 0.06
β_M	—	0.27 ± 0.04	0.43 ± 0.02	0.32 ± 0.04	—	0.24 ± 0.02	0.36 ± 0.02	0.30 ± 0.02
β_S	—	—	—	—	0.75 ± 0.10	0.65 ± 0.03	0.52 ± 0.03	0.53 ± 0.03
Scatter		0.32		0.43		0.14		0.25
α	7.70 ± 0.07	8.31 ± 0.04	8.91 ± 0.06	8.34 ± 0.04	8.57 ± 0.08	8.78 ± 0.09	9.05 ± 0.07	8.77 ± 0.04
$\beta_{A,\text{global}}$	0.47 ± 0.05	0.47 ± 0.02	0.38 ± 0.05	0.43 ± 0.03	0.31 ± 0.15	0.41 ± 0.11	0.52 ± 0.11	0.46 ± 0.08
β_S	—	—	—	—	0.75 ± 0.10	0.73 ± 0.04	0.71 ± 0.06	0.63 ± 0.03
Scatter		0.31		0.50		0.18		0.31

NOTE—The coefficients of the equations describe the relationship among molecular gas mass (M_{H_2}), SFR, stellar mass (M_\star), dust attenuation (A_V), and/or galaxy radius (R_{50}). Dust absorption is estimated from Balmer decrement in the fiber ($A_{V,\text{fiber}}$) or by galaxy-wide SED fitting ($A_{V,\text{global}}$). The scatter for the fits are quantified by the median absolute deviation (MAD, the left numbers corresponding to the median fits) and the root mean square deviation (RMSD, the right numbers corresponding to the mean fits).

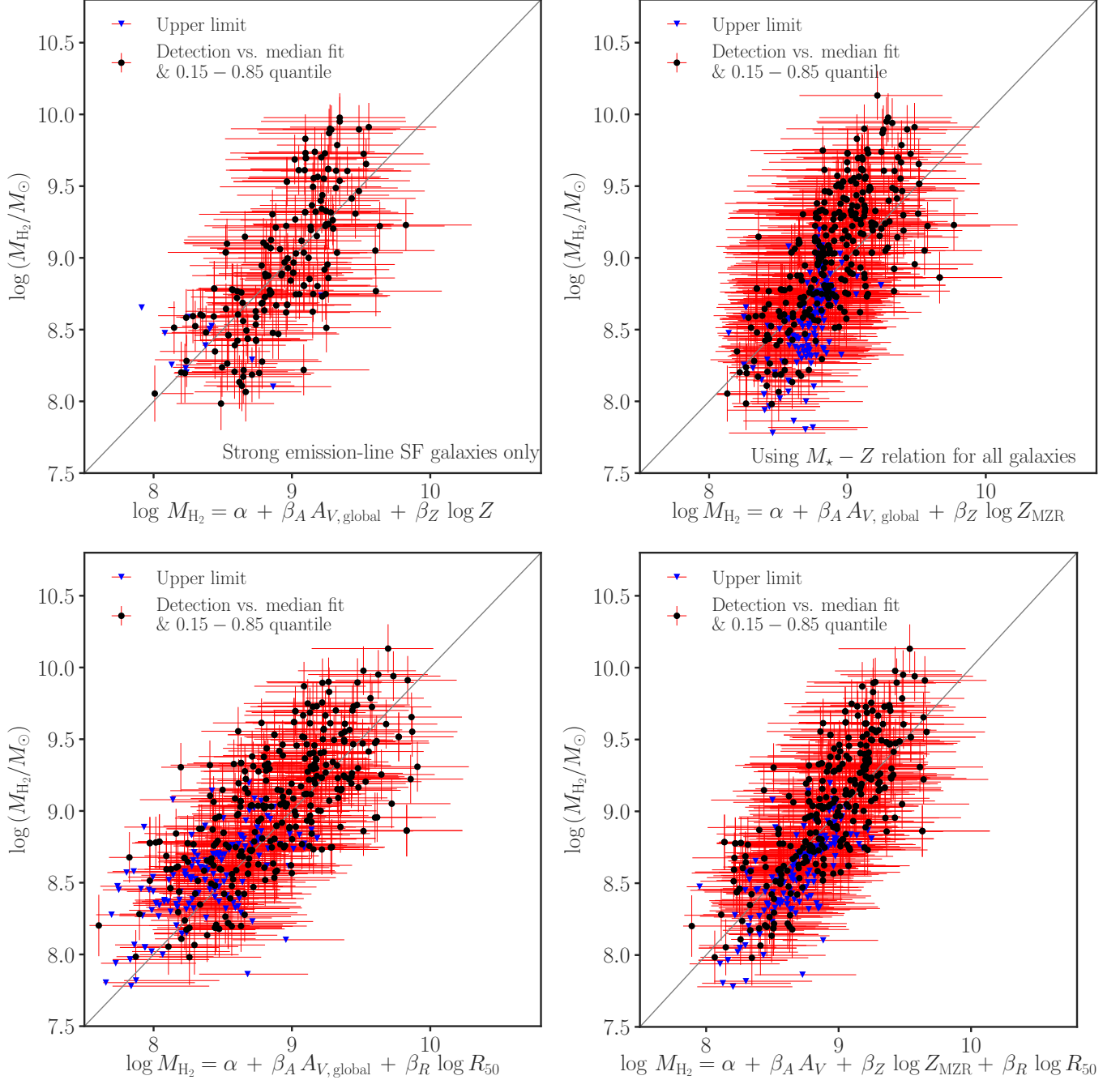


Figure 2. Similar to Figure 1, but here galaxy-wide stellar A_V is used.

$q = 0.15$ gas relations do not depend on i . Similarly, when A_V , metallicity (Z) and R_{50} are used i does not improve the gas mass prediction.

In conclusion, given other variables, the effect of inclination is marginal. The combination of A_V and Z or A_V and R_{50} is a better predictor of molecular gas than the combination of A_V and i . The latter combination, however, does marginally improve the fit of A_V by itself, more significantly in star-forming or gas-rich galaxies.

D. Comparison with the Herschel Reference Survey Data

The Herschel Reference Survey (HRS; Boselli et al. 2010) is a volume-limited ($D = 15\text{--}25$ Mpc) and K -band-selected sample of 322 galaxies. This sample has observations at 250, 350, and 500 μm , and is a benchmark for studies of dust

Table 5. Regression model fits for atomic gas, $\log M_{\text{HI}} = \alpha + \beta_A A_V + \beta_R \log R + \beta_M \log M_\star + \beta_S \log \text{SFR} + \beta_T \text{T types} + \beta_D \text{Prob. disk}$

	All Galaxies				Centrals Only			
	15%	Median	85%	Mean	15%	Median	85%	Mean
α	8.09 ± 0.17	8.58 ± 0.11	9.02 ± 0.05	8.54 ± 0.07	8.07 ± 0.35	8.52 ± 0.20	9.02 ± 0.06	8.50 ± 0.08
$\beta_{R_{90}}$	0.69 ± 0.20	0.98 ± 0.10	0.93 ± 0.05	0.98 ± 0.07	0.75 ± 0.24	1.05 ± 0.20	0.96 ± 0.06	1.04 ± 0.09
β_T	0.16 ± 0.01	0.06 ± 0.01	0.03 ± 0.01	0.05 ± 0.01	0.16 ± 0.06	0.06 ± 0.01	0.02 ± 0.01	0.05 ± 0.01
β_S	0.63 ± 0.05	0.44 ± 0.05	0.42 ± 0.02	0.40 ± 0.03	0.63 ± 0.12	0.46 ± 0.09	0.43 ± 0.07	0.42 ± 0.03
Scatter		0.22		0.39		0.22		0.39
α	8.40 ± 0.14	8.69 ± 0.12	9.08 ± 0.09	8.69 ± 0.07	8.18 ± 0.19	8.55 ± 0.07	9.01 ± 0.09	8.60 ± 0.08
$\beta_{R_{90}}$	0.72 ± 0.13	1.01 ± 0.13	0.94 ± 0.09	0.96 ± 0.08	1.02 ± 0.27	1.21 ± 0.07	1.05 ± 0.08	1.09 ± 0.09
β_S	0.77 ± 0.10	0.49 ± 0.06	0.42 ± 0.09	0.48 ± 0.03	0.75 ± 0.14	0.49 ± 0.06	0.41 ± 0.06	0.48 ± 0.03
Scatter		0.23		0.41		0.23		0.41
α	8.59 ± 0.04	9.07 ± 0.04	9.45 ± 0.04	9.04 ± 0.04	8.57 ± 0.05	9.02 ± 0.05	9.44 ± 0.05	9.01 ± 0.05
$\beta_{R_{50}}$	1.05 ± 0.11	1.08 ± 0.11	0.98 ± 0.07	1.03 ± 0.08	1.16 ± 0.07	1.20 ± 0.11	1.03 ± 0.10	1.12 ± 0.09
β_S	0.69 ± 0.05	0.47 ± 0.02	0.43 ± 0.05	0.44 ± 0.03	0.69 ± 0.07	0.47 ± 0.04	0.42 ± 0.10	0.45 ± 0.03
Scatter		0.23		0.41		0.24		0.41
α	12.32 ± 0.77	11.16 ± 0.71	9.18 ± 0.16	10.30 ± 0.43	11.34 ± 0.60	10.22 ± 0.48	9.16 ± 0.05	9.82 ± 0.50
$\beta_{A, \text{global}}$	0.97 ± 0.08	0.73 ± 0.23	0.33 ± 0.14	0.64 ± 0.08	0.63 ± 0.13	0.54 ± 0.11	0.29 ± 0.13	0.55 ± 0.10
$\beta_{R_{50}}$	2.42 ± 0.13	1.99 ± 0.20	1.09 ± 0.22	1.68 ± 0.11	2.47 ± 0.12	1.97 ± 0.13	1.18 ± 0.08	1.77 ± 0.12
β_M	-0.50 ± 0.09	-0.30 ± 0.08	—	-0.20 ± 0.05	-0.38 ± 0.07	-0.20 ± 0.05	—	-0.15 ± 0.05
Scatter		0.31		0.49		0.29		0.48
α	7.85 ± 0.08	8.41 ± 0.07	9.14 ± 0.07	8.49 ± 0.04	7.52 ± 0.20	8.42 ± 0.17	9.13 ± 0.05	8.47 ± 0.04
$\beta_{R_{50}}$	1.75 ± 0.43	1.06 ± 0.11	1.06 ± 0.23	1.06 ± 0.09	2.65 ± 0.44	1.32 ± 0.22	1.20 ± 0.10	1.28 ± 0.11
β_D	—	0.71 ± 0.05	0.26 ± 0.09	0.55 ± 0.05	—	0.52 ± 0.23	0.19 ± 0.06	0.45 ± 0.06
Scatter		0.29		0.47		0.28		0.47
α	7.48 ± 0.14	8.54 ± 0.06	9.18 ± 0.08	8.56 ± 0.04	7.44 ± 0.10	8.47 ± 0.08	9.13 ± 0.03	8.52 ± 0.04
$\beta_{R_{50}}$	1.94 ± 0.27	1.28 ± 0.19	1.17 ± 0.13	1.29 ± 0.09	2.08 ± 0.10	1.56 ± 0.17	1.30 ± 0.08	1.45 ± 0.10
β_T	0.16 ± 0.03	0.10 ± 0.01	0.03 ± 0.01	0.08 ± 0.01	0.15 ± 0.02	0.07 ± 0.02	0.03 ± 0.01	0.06 ± 0.01
Scatter		0.30		0.47		0.28		0.47
α	8.98 ± 0.06	9.55 ± 0.04	9.96 ± 0.03	9.50 ± 0.02	9.00 ± 0.14	9.55 ± 0.04	9.99 ± 0.03	9.51 ± 0.03
β_S	0.91 ± 0.08	0.66 ± 0.05	0.56 ± 0.03	0.60 ± 0.03	0.88 ± 0.17	0.67 ± 0.06	0.62 ± 0.05	0.65 ± 0.04
Scatter		0.30		0.49		0.29		0.48

NOTE—Subsets of the general equation are fitted. The notation is similar to Table 4. Morphology as quantified by T-types or disk probability is useful, in combination with radius, to predict atomic gas mass, when SFR is not used.

Table 6. Regression model fits for molecular gas, $\log M_{\text{H}_2} = \alpha + \beta_A A_V + \beta_R \log R_{50} + \beta_M \log M_\star + \beta_i(i - 56^\circ)$.

	A_V , Fiber				A_V , Global			
	15%	Median	85%	Mean	15%	Median	85%	Mean
α	9.30 ± 0.91	6.28 ± 0.48	6.33 ± 0.34	6.47 ± 0.43	12.32 ± 0.77	11.16 ± 0.71	6.48 ± 0.69	6.95 ± 0.40
β_A	0.45 ± 0.04	0.36 ± 0.03	0.38 ± 0.03	0.35 ± 0.03	0.97 ± 0.08	0.73 ± 0.23	1.32 ± 0.07	1.37 ± 0.08
β_R	1.61 ± 0.25	1.00 ± 0.10	0.60 ± 0.12	0.87 ± 0.11	2.42 ± 0.13	1.99 ± 0.20	0.89 ± 0.28	1.08 ± 0.10
β_M	-0.22 ± 0.10	0.16 ± 0.05	0.22 ± 0.03	0.15 ± 0.05	-0.50 ± 0.09	-0.30 ± 0.08	0.17 ± 0.08	0.07 ± 0.04
β_i	—	-0.004 ± 0.001	-0.006 ± 0.001	-0.003 ± 0.001	—	—	-0.005 ± 0.001	-0.003 ± 0.001
Scatter		0.23		0.40		0.24		0.37

NOTE—Here we add inclination, i , to the analysis in Table 4.

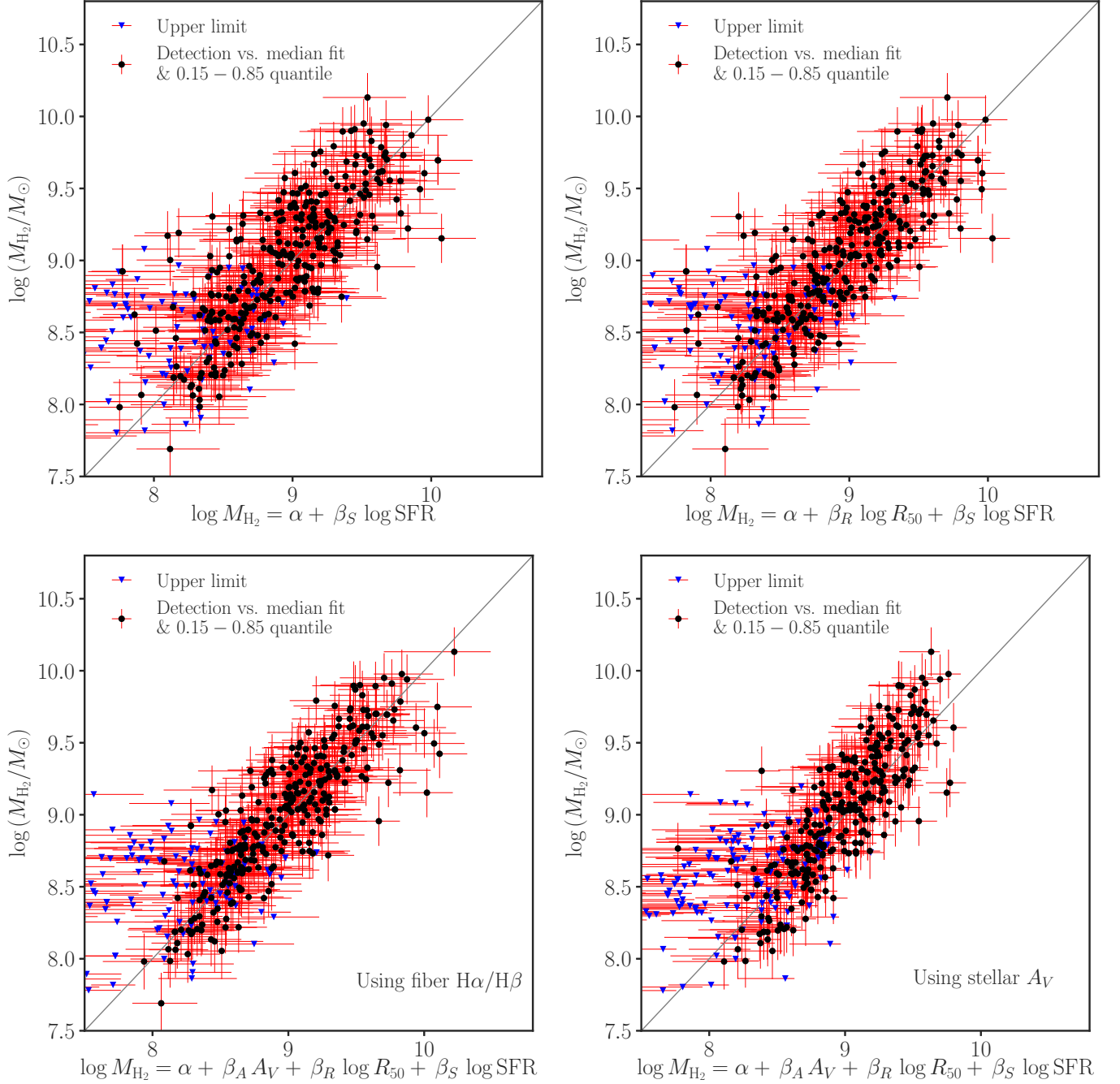


Figure 3. Scaling relations among molecular gas mass (M_{H_2}), A_V , R_{50} , and SFR. Adding R_{50} or A_V significantly improves to the primary correlation between M_{H_2} and SFR.

in the nearby universe. The sample spans a wide range of stellar mass ($M_* = 10^9 - 10^{11} M_\odot$), morphological types, and environments (from the field to the center of the Virgo Cluster).

We use the publicly available Herschel Database in Marseille⁸ to retrieve measurements of gas masses, SFR, and $\text{H}\alpha/\text{H}\beta$ of the HRS galaxies. Boselli et al. (2014a) obtained new CO (1–0) observations for 59 objects, which when combined with literature data produced a molecular gas catalog for 225 galaxies. Among these, only 158 have SFR measurements, and only 115 have both SFR and $\text{H}\alpha/\text{H}\beta$ measurements derived from long-slit spectroscopic observations. As shown in Figure 8, the massive quiescent HRS galaxies lack SFRs, and the xCOLD GASS sample we analyze

⁸ <https://hedam.lam.fr/HRS/>

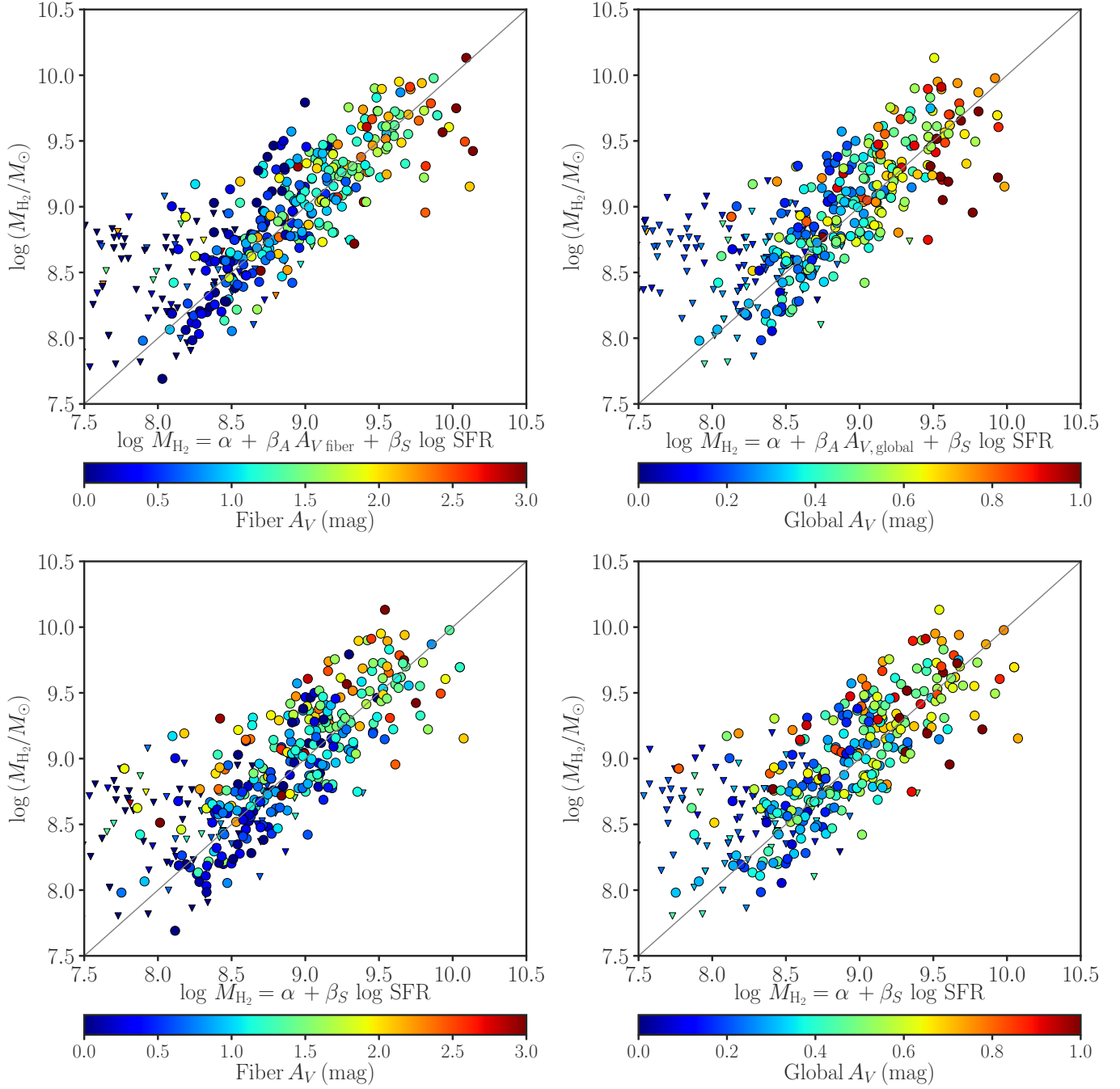


Figure 4. The top panels are the median relations with A_V and the bottom panels are without A_V .

in Section 3 is more representative in terms of coverage of the the M_{\star} vs. SFR plane. The SFRs of HRS were derived from a variety of available data (Boselli et al. 2015). We divide the SFRs by 1.58 to convert them to the Chabrier (2003) initial mass function. The aperture-corrected CO fluxes (with 3D exponential disk model) are converted to molecular gas masses using constant (Milky Way) and variable (H -band luminosity-dependent) X_{CO} conversion factors. Boselli et al. (2014a) also compiled H I data for 315 HRS galaxies from the literature. For 52 H I non-detections, 5σ upper limits were estimated assuming a velocity width of 300 km s^{-1} . Likewise, for the 82 H_2 non-detections, 5σ upper limits were estimated by assuming a CO velocity width equal to the H I width, when detected, or to 300 km s^{-1} otherwise. Stellar masses and r -band half-light radii were taken from Cortese et al. (2012). The stellar masses

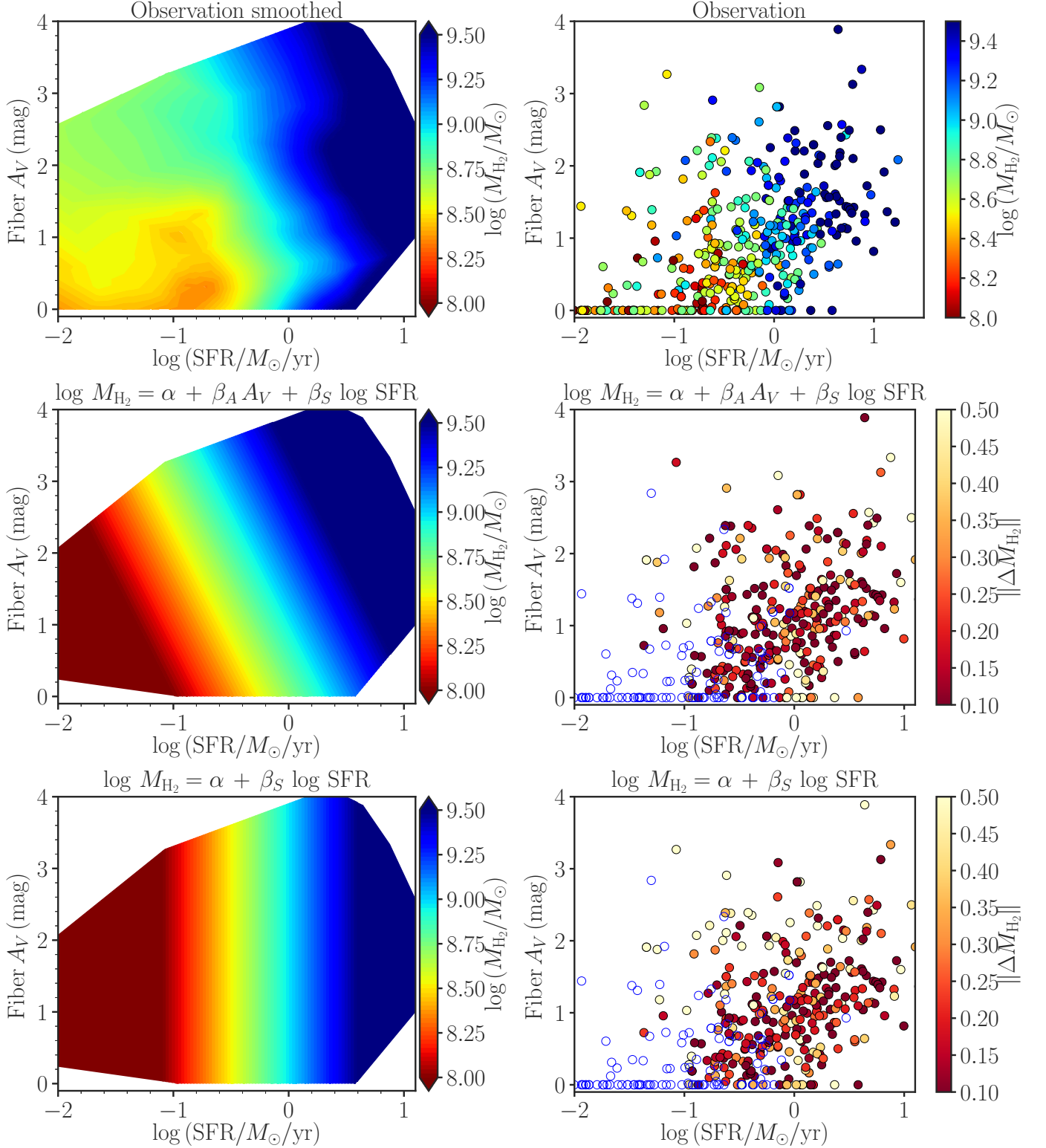


Figure 5. The molecular gas mass has a secondary dependence on A_V , in addition to SFR. The top panels show trends in the observed data. The top left panel is LOESS-smoothed (Cappellari et al. 2013) using 20% of the data in the local approximation. Note that almost all data points below $1 M_\odot \text{ yr}^{-1}$ are upper limits, and the smoothing does not treat these points differently. The figure The middle panels show the median fit and its residuals with A_V . The bottom panels show the median fit and its residuals without A_V . The open blue circles are non-detections.

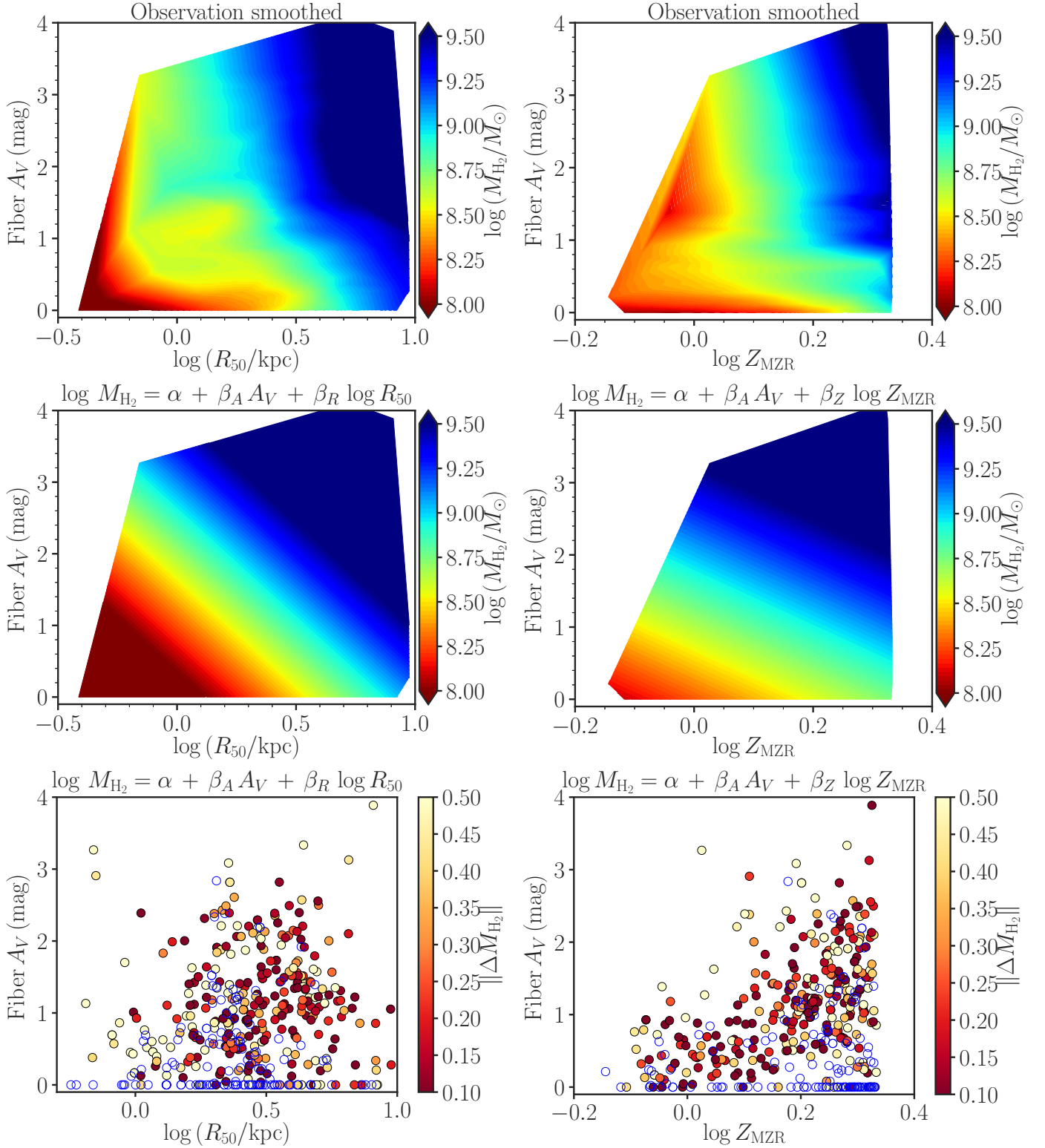


Figure 6. Similar to Figure 5 but here the dependence of M_{H_2} on A_V , inferred metallicity ($\log Z_{\text{MZR}} = 12 + \log [\text{O}/\text{H}] - 8.8$), and R_{50} is shown. The mean gas-phase metallicity is estimated from the mass-metallicity relation (Tremonti et al. 2004).

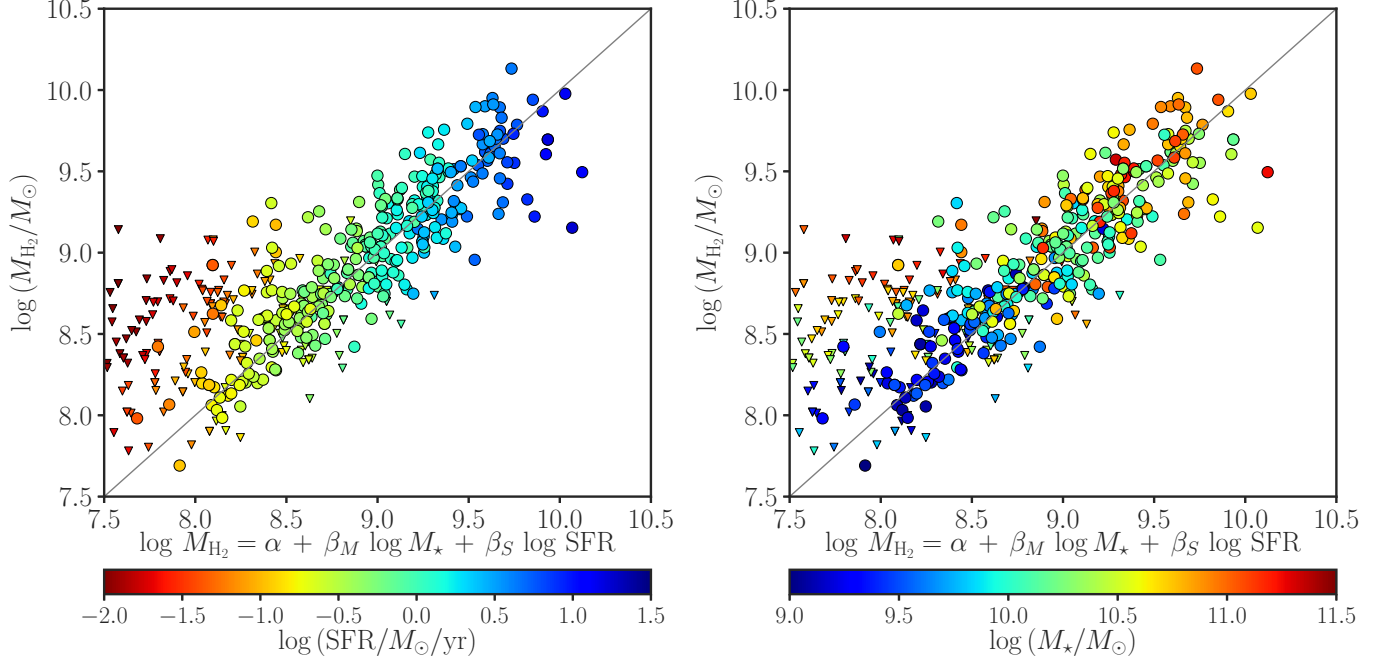


Figure 7. The median molecular gas mass predicted by M_* and SFR. The left panel is color-coded by SFR, while the right panel is color-coded by M_* . The right panel shows that combining M_* with SFR fails to predict molecular gas masses of gas-poor galaxies (see upper panels of Figure 4).

were derived from i -band luminosities using a relation between $g - i$ color and stellar mass-to-light ratio, assuming a Chabrier initial mass function.

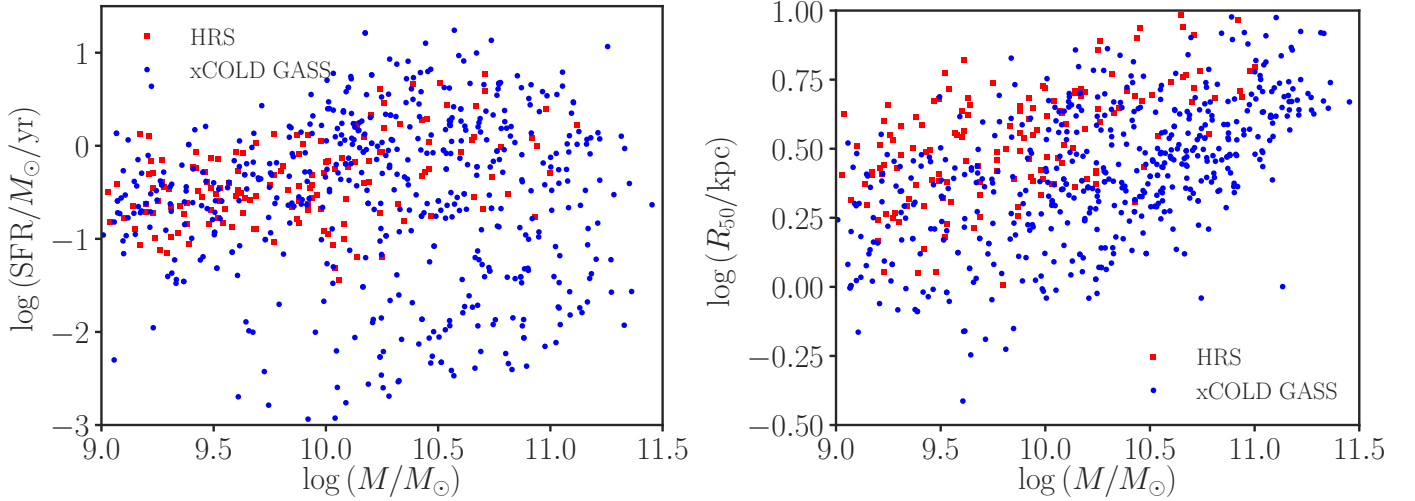
Boselli et al. (2014b) used the HRS sample and scaling variables M_* , stellar surface density, specific star formation rate $\text{SSFR} \equiv \text{SFR}/M_*$, and metallicity to extend the gas scaling relations for massive galaxies in COLD GASS (which is the precursor to xCOLD GASS, Saintonge et al. 2011). They found a significant correlation between M_{H_2}/M_* and SSFR and between $M_{\text{H}_2}/M_{\text{HI}}$ and metallicity. Here we also do a regression analysis of the HRS sample using M_* and SFR as independent variables and M_{H_2} as dependent variable. As shown in Table 7, once the SFR dependence is taken into an account, the M_* dependence (for the mean relation) is much weaker for this sample compared to xCOLD GASS (Table 4). Furthermore, for late-type galaxies, Boselli et al. (2014b) found $\log M_{\text{H}_2}/M_* \propto a \log \text{SSFR}$, where $a = 0.94$ for a constant X_{CO} and $a = 1.01$ for a luminosity-dependent X_{CO} (see their Table 3). As $\log M_{\text{H}_2} \propto (1 - a) \log M_* + a \log \text{SFR}$, their fit can be interpreted as indicating that the mass dependence is very weak. Thus, for the HRS sample the M_{H_2}/M_* vs. SSFR relation is similar to the M_{H_2} vs. SFR relation. Boselli et al.’s method of fitting—using M_* on both sides—may induce correlations in the residuals, in addition to forcing SFR and M_* to share correlated coefficients for the mean gas mass relation. Because the method is implicit, it does not allow physical insights to be gleaned from the coefficients of SFR and M_* separately. In any event, our fits for the xCOLD GASS/xGASS data are not inconsistent with the HRS sample (Figures 9 and 10), despite the difference in the two samples, the X_{CO} used, and how SFR and A_V are measured.

Similar to Boselli et al. (2014b), Saintonge et al. (2017) found that M_{H_2}/M_* shows the tightest correlation with SSFR for xCOLD GASS data. Unlike previous work that use these data, we include the upper limits in our analysis and give simple and convenient formulae summarizing the data. We also present scaling relations, for the first time, that do not use SFR. Despite the emphasis of previous scaling relations on M_* , Tables 1 and 4 show that the improvement brought by a linear term of M_* is small if half-light radius is used. Using Random Forest, we confirm that A_V and R_{50} have better predictive power than M_* . The scaling relations in the literature using the equivalent (rearranged) relation may give the impression that they have lower dispersions because they did not include upper limits in their analyses. In addition, the M_{H_2}/M_* -SSFR relation in Boselli et al. (2014b) looks tighter because the galaxies in their sample with molecular gas measurements are preferentially star-forming, unlike the galaxies in xCOLD GASS, which contains many quiescent galaxies. Nearly all quiescent galaxies in xCOLD GASS are upper limits, and these upper limits have less constraining power when M_* is combined with SFR (e.g., Figure 7). Note also that xCOLD GASS/xGASS gives

Table 7. Regression model fits for the Herschel Reference Survey (HRS) data, $\log M_{\text{H}_2} = \alpha + \beta_M \log M_\star + \beta_S \log \text{SFR}$.

	$X_{\text{CO,MW}}$				Variable X_{CO}			
	15%	Median	85%	Mean	15%	Median	85%	Mean
α	8.43 ± 0.3	5.89 ± 0.07	5.45 ± 1.40	8.67 ± 0.19	8.38 ± 0.12	8.19 ± 0.58	8.50 ± 0.14	8.72 ± 0.16
β_M	0.018 ± 0.004	0.32 ± 0.07	0.39 ± 0.14	0.04 ± 0.02	0.018 ± 0.004	0.08 ± 0.07	0.07 ± 0.13	0.02 ± 0.02
β_S	0.65 ± 0.28	0.70 ± 0.08	0.65 ± 0.14	0.43 ± 0.08	0.46 ± 0.19	0.59 ± 0.08	0.57 ± 0.12	0.58 ± 0.06
Scatter		0.17		0.39		0.17		0.33

NOTE—The median relation of the HRS sample for the case of $X_{\text{CO,MW}}$ (a constant Milky Way value) is similar to that of the xCOLD GASS sample. In the latter sample, the fits do not change much depending on X_{CO} .

**Figure 8.** Comparison of the Herschel Reference Survey data (Boselli et al. 2010) with xCOLD GASS (Saintonge et al. 2017). SFR measurements are lacking for massive quiescent HRS galaxies.

3σ upper limits, while HRS uses 5σ upper limits, which further reinforces the impression that the scatter is small because the upper limits overlap with the detections. Lastly, adding M_\star , in almost all cases, does not statistically significantly improve the prediction of atomic gas masses.

References

- Accurso, G., Saintonge, A., Catinella, B., et al. 2017, *MNRAS*, 470, 4750
Aguado, D. S., Ahumada, R., Almeida, A., et al. 2019, *ApJS*, 240, 23
Akritas, M. G., & Siebert, J. 1996, *MNRAS*, 278, 919
Aoyama, S., Hou, K.-C., Shimizu, I., et al. 2017, *MNRAS*, 466, 105
Bekki, K. 2013, *Monthly Notices of the Royal Astronomical Society*, 432, 2298
—. 2015, *Monthly Notices of the Royal Astronomical Society*, 449, 1625
Berta, S., Lutz, D., Genzel, R., Förster-Schreiber, N. M., & Tacconi, L. J. 2016, *A&A*, 587, A73
Bertemes, C., Wuyts, S., Lutz, D., et al. 2018, *MNRAS*, 478, 1442
Bigiel, F., & Blitz, L. 2012, *ApJ*, 756, 183
Blitz, L., & Rosolowsky, E. 2006, *ApJ*, 650, 933
Boissier, S., Boselli, A., Buat, V., Donas, J., & Milliard, B. 2004, *A&A*, 424, 465
Boissier, S., Gil de Paz, A., Boselli, A., et al. 2007, *ApJS*, 173, 524
Bolatto, A. D., Wolfire, M., & Leroy, A. K. 2013, *ARA&A*, 51, 207
Boselli, A., Cortese, L., & Boquien, M. 2014a, *A&A*, 564, A65
Boselli, A., Cortese, L., Boquien, M., et al. 2014b, *A&A*, 564, A66
Boselli, A., Fossati, M., Gavazzi, G., et al. 2015, *Astronomy and Astrophysics*, 579, A102
Boselli, A., Eales, S., Cortese, L., et al. 2010, *PASP*, 122, 261

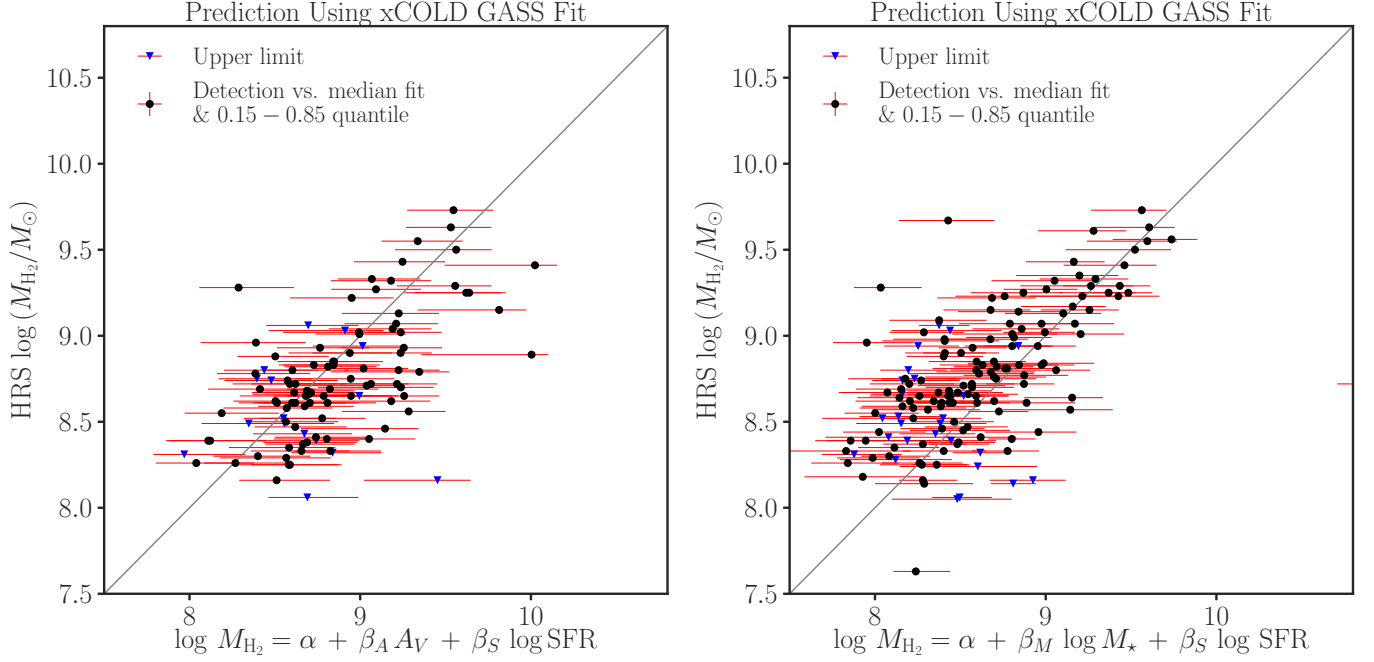


Figure 9. Scaling relations of molecular gas derived from xCOLD GASS data are consistent with independent observations of molecular gas of HRS galaxies.

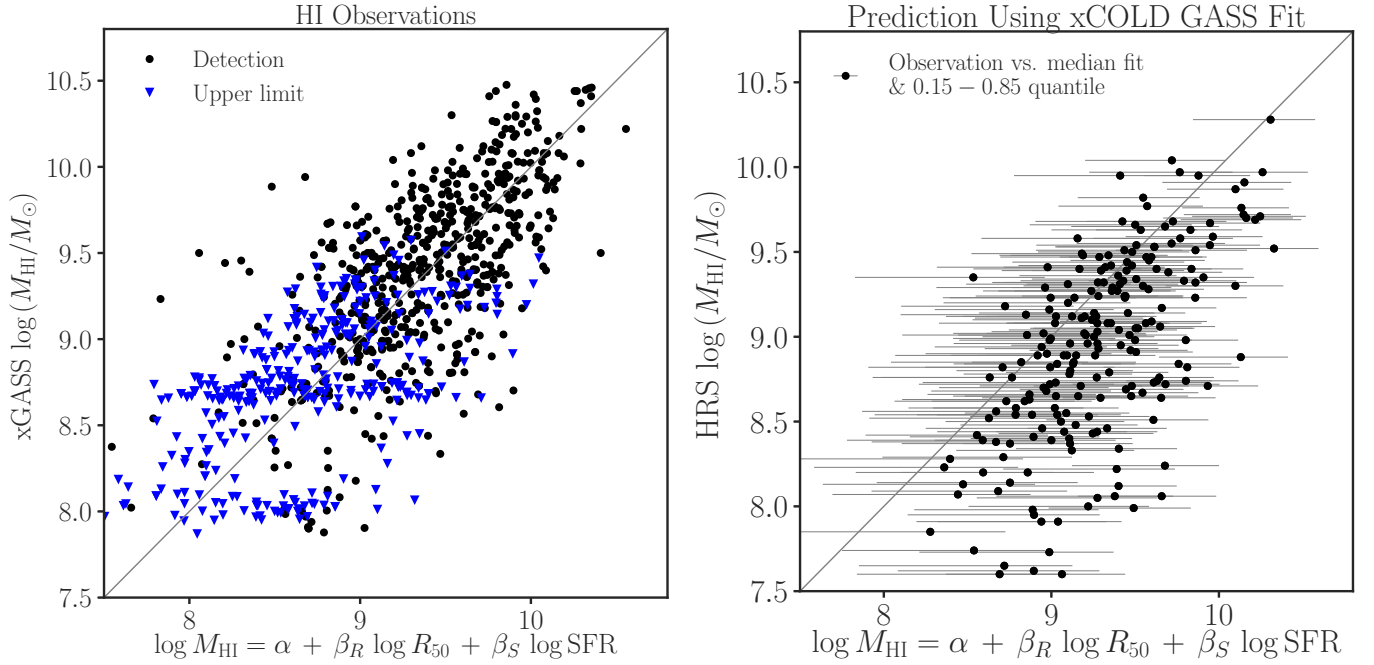


Figure 10. The left panel shows our median fit for atomic gas data of the xGASS sample. Our prediction using this fit is consistent with the observed atomic gas masses of galaxies in HRS.

- Bouché, N., Dekel, A., Genzel, R., et al. 2010, *ApJ*, 718, 1001
 Brinchmann, J., Charlot, S., Kauffmann, G., et al. 2013, *Monthly Notices of the Royal Astronomical Society*, 432, 2112
 Calzetti, D., Kinney, A. L., & Storchi-Bergmann, T. 1994, *ApJ*, 429, 582
 Cappellari, M., McDermid, R. M., Alatalo, K., et al. 2013, *MNRAS*, 432, 1862
 Casasola, V., Cassarà, L. P., Bianchi, S., et al. 2017, *A&A*, 605, A18
 Catinella, B., Saintonge, A., Janowiecki, S., et al. 2018, *MNRAS*, 476, 875

- Chabrier, G. 2003, *Publications of the Astronomical Society of the Pacific*, 115, 763
- Charlot, S., & Fall, S. M. 2000, *ApJ*, 539, 718
- Chary, R., & Elbaz, D. 2001, *ApJ*, 556, 562
- Chiang, I. D., Sandstrom, K. M., Chasteney, J., et al. 2018, *ApJ*, 865, 117
- Concas, A., & Popesso, P. 2019, *MNRAS*, arXiv:1905.02214
- Corbelli, E., Bianchi, S., Cortese, L., et al. 2012, *Astronomy and Astrophysics*, 542, A32
- Cortese, L., Boissier, S., Boselli, A., et al. 2012, *A&A*, 544, A101
- De Vis, P., Jones, A., Viaene, S., et al. 2019, *A&A*, 623, A5
- Dekel, A., Sari, R., & Ceverino, D. 2009, *ApJ*, 703, 785
- Dekel, A., Zolotov, A., Tweed, D., et al. 2013, *MNRAS*, 435, 999
- Devereux, N. A., & Young, J. S. 1990, *ApJ*, 359, 42
- Diemer, B., Stevens, A. R. H., Lagos, C. d. P., et al. 2019, arXiv e-prints, arXiv:1902.10714
- Domínguez Sánchez, H., Huertas-Company, M., Bernardi, M., Tuccillo, D., & Fischer, J. L. 2018, *MNRAS*, 476, 3661
- Draine, B. T., Dale, D. A., Bendo, G., et al. 2007, *ApJ*, 663, 866
- Eales, S., Smith, M. W. L., Auld, R., et al. 2012, *ApJ*, 761, 168
- Faucher-Giguère, C.-A., Quataert, E., & Hopkins, P. F. 2013, *MNRAS*, 433, 1970
- Feigelson, E. D., & Nelson, P. I. 1985, *ApJ*, 293, 192
- Ferland, G. J., & Netzer, H. 1983, *ApJ*, 264, 105
- Fernández, X., Gim, H. B., van Gorkom, J. H., et al. 2016, *ApJL*, 824, L1
- Forbes, J. C., Krumholz, M. R., Burkert, A., & Dekel, A. 2014, *MNRAS*, 443, 168
- Freundlich, J., Combes, F., Tacconi, L. J., et al. 2019, *A&A*, 622, A105
- Galametz, M., Madden, S. C., Galliano, F., et al. 2011, *A&A*, 532, A56
- Galliano, F., Galametz, M., & Jones, A. P. 2018, *ARA&A*, 56, 673
- Gaskell, C. M., & Ferland, G. J. 1984, *PASP*, 96, 393
- Genzel, R., Tacconi, L. J., Lutz, D., et al. 2015, *ApJ*, 800, 20
- Giannetti, A., Leurini, S., König, C., et al. 2017, *A&A*, 606, L12
- Glover, S. C. O., & Clark, P. C. 2012, *MNRAS*, 421, 9
- Gong, M., Ostriker, E. C., & Wolfire, M. G. 2017, *ApJ*, 843, 38
- Groves, B. A., Schinnerer, E., Leroy, A., et al. 2015, *ApJ*, 799, 96
- Harrison, C. M., Costa, T., Tadhunter, C. N., et al. 2018, *Nature Astronomy*, 2, 198
- Haynes, M. P., Giovanelli, R., Kent, B. R., et al. 2018, *ApJ*, 861, 49
- Helsel, D. R. 2012, *Statistics for Censored Environmental Data Using Minitab and R*
- Hess, K. M., Luber, N. M., Fernández, X., et al. 2019, *MNRAS*, 484, 2234
- Hopkins, P. F., Kereš, D., Oñorbe, J., et al. 2014, *MNRAS*, 445, 581
- Hopkins, P. F., Quataert, E., & Murray, N. 2011, *MNRAS*, 417, 950
- Hou, K.-C., Aoyama, S., Hirashita, H., Nagamine, K., & Shimizu, I. 2019, *MNRAS*, 485, 1727
- Issa, M. R., MacLaren, I., & Wolfendale, A. W. 1990, *A&A*, 236, 237
- Janowiecki, S., Cortese, L., Catinella, B., & Goodwin, A. J. 2018, *MNRAS*, 476, 1390
- Kahre, L., Walterbos, R. A., Kim, H., et al. 2018, *ApJ*, 855, 133
- Kravtsov, A. V. 2013, *ApJL*, 764, L31
- Kreckel, K., Groves, B., Schinnerer, E., et al. 2013, *ApJ*, 771, 62
- Krumholz, M. R., Leroy, A. K., & McKee, C. F. 2011, *ApJ*, 731, 25
- Leroy, A. K., Bolatto, A., Gordon, K., et al. 2011, *ApJ*, 737, 12
- Li, Q., Narayanan, D., & Davé, R. 2019, arXiv e-prints, arXiv:1906.09277
- Lilly, S. J., Carollo, C. M., Pipino, A., Renzini, A., & Peng, Y. 2013, *ApJ*, 772, 119
- Lisenfeld, U., & Ferrara, A. 1998, *ApJ*, 496, 145
- Mattsson, L., & Andersen, A. C. 2012, *Monthly Notices of the Royal Astronomical Society*, 423, 38
- Mo, H. J., Mao, S., & White, S. D. M. 1998, *MNRAS*, 295, 319
- Muñoz-Mateos, J. C., Gil de Paz, A., Boissier, S., et al. 2009, *ApJ*, 701, 1965
- Nair, P. B., & Abraham, R. G. 2010, *ApJS*, 186, 427
- Noeske, K. G., Weiner, B. J., Faber, S. M., et al. 2007, *ApJ*, 660, L43
- Obreschkow, D., & Rawlings, S. 2009, *Monthly Notices of the Royal Astronomical Society*, 394, 1857
- Ostriker, E. C., & Shetty, R. 2011, *ApJ*, 731, 41
- Pappalardo, C., Bianchi, S., Corbelli, E., et al. 2012, *A&A*, 545, A75
- Peng, Y.-j., & Maiolino, R. 2014, *MNRAS*, 443, 3643
- Popping, G., Caputi, K. I., Trager, S. C., et al. 2015, *MNRAS*, 454, 2258
- Portnoy, S. 2003, *Journal of the American Statistical Association*, 98, 1001
- Rémy-Ruyer, A., Madden, S. C., Galliano, F., et al. 2014, *A&A*, 563, A31
- Rodríguez-Puebla, A., Primack, J. R., Behroozi, P., & Faber, S. M. 2016, *MNRAS*, 455, 2592
- Saintonge, A., Kauffmann, G., Kramer, C., et al. 2011, *Monthly Notices of the Royal Astronomical Society*, 415, 32
- Saintonge, A., Catinella, B., Tacconi, L. J., et al. 2017, *ApJS*, 233, 22
- Salim, S., Boquien, M., & Lee, J. C. 2018, *ApJ*, 859, 11
- Salim, S., Lee, J. C., Janowiecki, S., et al. 2016, *ApJS*, 227, 2
- Sandstrom, K. M., Leroy, A. K., Walter, F., et al. 2013, *ApJ*, 777, 5
- Schruba, A., Leroy, A. K., Walter, F., et al. 2011, *AJ*, 142, 37

- Scoville, N., Sheth, K., Aussel, H., et al. 2016, *ApJ*, 820, 83
- Shangguan, J., Ho, L. C., Li, R., et al. 2019, *ApJ*, 870, 104
- Shangguan, J., Ho, L. C., & Xie, Y. 2018, *ApJ*, 854, 158
- Simard, L., Mendel, J. T., Patton, D. R., Ellison, S. L., & McConnachie, A. W. 2011, *ApJS*, 196, 11
- Smith, M. W. L., Eales, S. A., De Looze, I., et al. 2016, *MNRAS*, 462, 331
- Tremonti, C. A., Heckman, T. M., Kauffmann, G., et al. 2004, *ApJ*, 613, 898
- Verheijen, M., van Gorkom, J. H., Szomoru, A., et al. 2007, *ApJL*, 668, L9
- Vílchez, J. M., Relaño, M., Kennicutt, R., et al. 2019, *MNRAS*, 483, 4968
- Wang, J., Fu, J., Aumer, M., et al. 2014, *MNRAS*, 441, 2159
- Wild, V., Charlot, S., Brinchmann, J., et al. 2011, *MNRAS*, 417, 1760
- Willett, K. W., Lintott, C. J., Bamford, S. P., et al. 2013, *MNRAS*, 435, 2835
- Yang, X., Mo, H. J., van den Bosch, F. C., et al. 2007, *ApJ*, 671, 153
- Yesuf, H. M., French, K. D., Faber, S. M., & Koo, D. C. 2017, *MNRAS*, 469, 3015
- Zhukovska, S. 2014, *Astronomy and Astrophysics*, 562, A76